

# **Direct Tension Testing of 8-in. (200-mm) Diameter TR-XTREME™ Ductile Iron Pipe**

**Shih-Hung Chiu**

**Qinglai Zhang**

**Shakhzod Takhirov**

**Kenichi Soga**



**Berkeley**  
**CENTER FOR**  
**Smart Infrastructure**

CSI Report 2023/01  
Center for Smart Infrastructure (CSI)  
Department of Civil and Environmental Engineering  
University of California, Berkeley January 2023

## EXECUTIVE SUMMARY

This report describes the results of full-scale experimental studies and finite element modeling of two 8-inch TR-XTREME™ ductile iron pipes manufactured by US Pipe. The pipe's performance under direct tension force was studied. The pipe was designed to maintain a full-service life even after seismic events to improve seismic resiliency. The lab tests were conducted under a monotonically increasing axial force up to severe damage to the pipe or significant water leakage. The pipe and the joint were extensively instrumented by conventional sensors (strain gages and position transducers) and novel fiber optic sensors. The performance of the finite element model was validated using the experimental results obtained from distributed fiber optic sensors, which can be used as the reference model for future related pipeline research, including but not limited to parametric study and experimental tests.

**Keywords:** *Ductile iron pipe, water pipelines, fiber optic sensing, leakage, full-scale testing, finite element analysis.*

## **ACKNOWLEDGMENTS**

The funding for this project was provided by the East Bay Municipal Utility District (EBMUD), and the pipes used for the experiment were supplied by US Pipe. The completion of the work would not be possible without the support of Llyr Griffith, John Kochan, and Phillip Wong of the University of California, Berkeley. Active involvement and guidance from Jeff Mason of US Pipe and David Katzev of EBMUD are greatly appreciated. The authors would like to acknowledge Dr. Brad Wham of the University of Colorado Boulder and Dr. Blake Berger of Thornton Tomasetti for their active participation in the project.

## **DISCLAIMER**

Any opinions, findings, conclusions, or recommendations expressed in this material are those of the author(s) and do not necessarily reflect those of the University of California, Berkeley.

# CONTENTS

<b>EXECUTIVE SUMMARY</b> .....	<b>II</b>
<b>ACKNOWLEDGMENTS</b> .....	<b>III</b>
<b>DISCLAIMER</b> .....	<b>IV</b>
<b>CONTENTS</b> .....	<b>V</b>
<b>LIST OF FIGURES</b> .....	<b>VI</b>
<b>LIST OF TABLES</b> .....	<b>VIII</b>
<b>1 Introduction</b> .....	<b>9</b>
<b>2 Experimental Setup</b> .....	<b>11</b>
<b>3 Specimen List and Instrumentation</b> .....	<b>13</b>
<b>3.1 Test Specimens</b> .....	<b>13</b>
<b>3.2 Instrumentation</b> .....	<b>14</b>
3.2.1 Conventional Instruments.....	15
3.2.2 Fiber Optic Sensors.....	17
<b>4 Test results</b> .....	<b>21</b>
<b>4.1 Test Data Analysis</b> .....	<b>21</b>
4.1.1 Axial Strains .....	22
4.1.2 Hoop Strains .....	25
<b>4.2 Failure Modes</b> .....	<b>29</b>
<b>5 Finite Element Analysis</b> .....	<b>31</b>
<b>5.1 Overview of Numerical Model</b> .....	<b>31</b>
<b>5.2 Determination of Pipe Parameters</b> .....	<b>32</b>
<b>5.3 FEM Results</b> .....	<b>32</b>
5.3.1 Comparison of the FE Model and Experimental Data for Specimen 1 .....	35
5.3.2 Comparison of the FE Model and Experimental Data for Specimen 2 .....	37
<b>6 Conclusions</b> .....	<b>41</b>
<b>7 References</b> .....	<b>41</b>
<b>Appendix A: Fiber Optic Sensors Result</b> .....	<b>42</b>
(a) Specimen 1 .....	42
(b) Specimen 2 .....	48
<b>Appendix B: Comparison of FE simulation results and experimental results</b> .....	<b>54</b>
(a) Specimen 1 .....	54
(b) Specimen 2 .....	56

## LIST OF FIGURES

Figure 1-1 Schematic drawing of TR-XTREME™ joint (U.S. Pipe, 2020).....	9
Figure 1-2 Recommended three installation positions (U.S. Pipe, 2020).....	10
Figure 2-1 Experiment setup.....	11
Figure 2-2 Overview of experiment setup .....	12
Figure 2-3 Locking segments and rubber gasket .....	12
Figure 3-1 Welded features at the ends of the two specimens.....	13
Figure 3-2 Instrumentation plan of conventional instruments.....	14
Figure 3-3 Instrumentation plan of fiber optic sensors.....	18
Figure 3-4 Circumferential sensor locations.....	19
Figure 3-5 Illustration of adhesive location of cables in the longitudinal direction .....	20
Figure 4-1 Comparison of the tests.....	21
Figure 4-2 Axial strain vs axial force of Specimen 1 .....	22
Figure 4-3 Axial strain vs axial force of Specimen 2 .....	22
Figure 4-4 Strain development of Specimens 1 in longitudinal direction under 170-kip loading condition. (a) West side of bell pipe, (b) Top side of bell pipe, (c) West side of spigot, (d) Top side of spigot .....	23
Figure 4-5 Strain development of Specimen 2 in longitudinal direction under 170-kip loading condition. (a) West side of bell pipe, (b) Top side of bell pipe, (c) West side of spigot, (d) Top side of spigot .....	24
Figure 4-6 Bell failure mechanism .....	25
Figure 4-7 Hoop strain vs axial force of Specimen 1 .....	26
Figure 4-8 Hoop strain vs axial force of Specimen 2 .....	26
Figure 4-9 Strain distribution in the circumferential direction under 170-kip loading condition of Specimen 1. (a) sensor on the bell pipe (b) sensor at the mid location of bell (c) sensor on top of the locking segments on the bell (d) sensor on the spigot.....	27
Figure 4-10 Strain distribution in circumferential direction under 170-kip loading condition of Specimen 2. (a) sensor on the bell pipe (b) sensor at the mid location of bell (c) sensor on top of the locking segments on the bell (d) sensor on the spigot .....	28
Figure 4-11 Failure of the weld bead at the end of the pipe of Specimen 1 .....	29
Figure 4-12 Failure of Bell of Specimen 2 .....	30
Figure 4-13 Load and water pressure versus average joint opening of Specimen 2.....	30
Figure 5-1 Three main parts in the FE model .....	31
Figure 5-2 3-D FE model mesh for axial tension test.....	32
Figure 5-3 Comparison of FEM result and experimental result of test 2 .....	33
Figure 5-4 The stress contours of deformed joint at applied: (a) displacement=2 inches; (b) displacement=2.4 inches; (c) displacement=2.9 inches;.....	33
Figure 5-5 Sectional view of joint rotation.....	34
Figure 5-6 Damage area comparison .....	34
Figure 5-7 Numerical simulation showing (a) axial tension stress S33; (b) circumferential stress S22 (c) shear stress S23 at 2.4 in. of axial displacement in cylindrical coordinates .....	35
Figure 5-8 Comparison of hoop strain results from FE simulation and experiment under 185-kip loading condition of test 1. (a) sensor on the bell pipe (b) sensor at the mid location of bell (c) sensor on top of the locking segments on the bell (d) sensor on the spigot .....	36
Figure 5-9 Comparison of axial strain results from FE simulation and experiment under 185-kip loading condition of test 1. (a) West side of bell pipe, (b) Top side of bell pipe, (c) West side of spigot, (d) Top side of spigot .....	37
Figure 5-10 Comparison of axial strain results from FE simulation and experiment under 125-kip loading condition of test 2. (a) sensor on the bell pipe (b) sensor at the mid location of bell (c) sensor on top of the locking segments on the bell (d) sensor on the spigot .....	38
Figure 5-11 Comparison of axial strain results from FE simulation and experiment under 125-kip loading condition of test 2. (a) West side of bell pipe, (b) Top side of bell pipe, (c) West side of spigot, (d) Top side of spigot .....	39

Figure 5-12 Comparison of hoop strain results from FE simulation and experiment under 170-kip loading condition of test 2. (a) sensor on the bell pipe (b) sensor at the mid location of bell (c) sensor on top of the locking segments on the bell (d) sensor on the spigot ..... 39

Figure 5-13 Comparison of axial strain results from FE simulation and experiment under 170-kip loading condition of test 2. (a) West side of bell pipe, (b) Top side of bell pipe, (c) West side of spigot, (d) Top side of the spigot..... 40

## LIST OF TABLES

Table 3-1 Test log .....	13
Table 3-2 Exact location of the conventional instruments.....	15
Table 3-3 Conventional instrumentation for U.S. Pipe TR-XTREME™ Joint tension test.....	15
Table 3-4 Schematic illustration of the selected strain sensor cable (Wu et al., 2015) .....	17
Table 3-5 Fiber optic sensors for U.S. Pipe TR-XTREME™ Joint tension test .....	19
Table 3-6 Exact location of the fiber optic circumferential sensors .....	19
Table 3-7 Adhesive location of longitudinal direction cables of Specimen 1 .....	20
Table 4-1 Summary of the tests .....	30
Table 5-1 Ductile iron pipe properties.....	32



# 1 Introduction

This report summarizes the experimental and finite element modeling results of the direct tension tests performed on two 8-inch TR-XTREME™ ductile iron pipe (Class 53) specimens manufactured by US Pipe. The pipe was designed to maintain the full water service after seismic events to achieve the seismic resiliency of pipeline systems. Based on the specifications of the manufacturer (U.S. Pipe, 2020), the joint of the pipe provides a total of 2.9 inches of axial travel and a 5-degree rotation capacity. The main components of the joint are shown in the schematic drawing in Figure 1-1. The spigot is designed to be inserted into a bell, passing through a rubber gasket, and is equipped with a weld bead to bear against the locking segments, used as a locking mechanism while pulling. The slot for inserting the locking segments is located at the top of the bell. After placing all segments, a rubber insert is installed on top to have a spring load compressing all segments together. Three white stripes on the spigot are used to indicate the installation position along the pipe. The manufacturer recommends three installation positions: collapsed, midpoint, and extended location, as shown in Figure 1-2. Collapsed and Midpoint installation positions were used for the experiments in this study. A direct tension test was conducted to test the capacity of the bell under a monotonically increasing tension force.

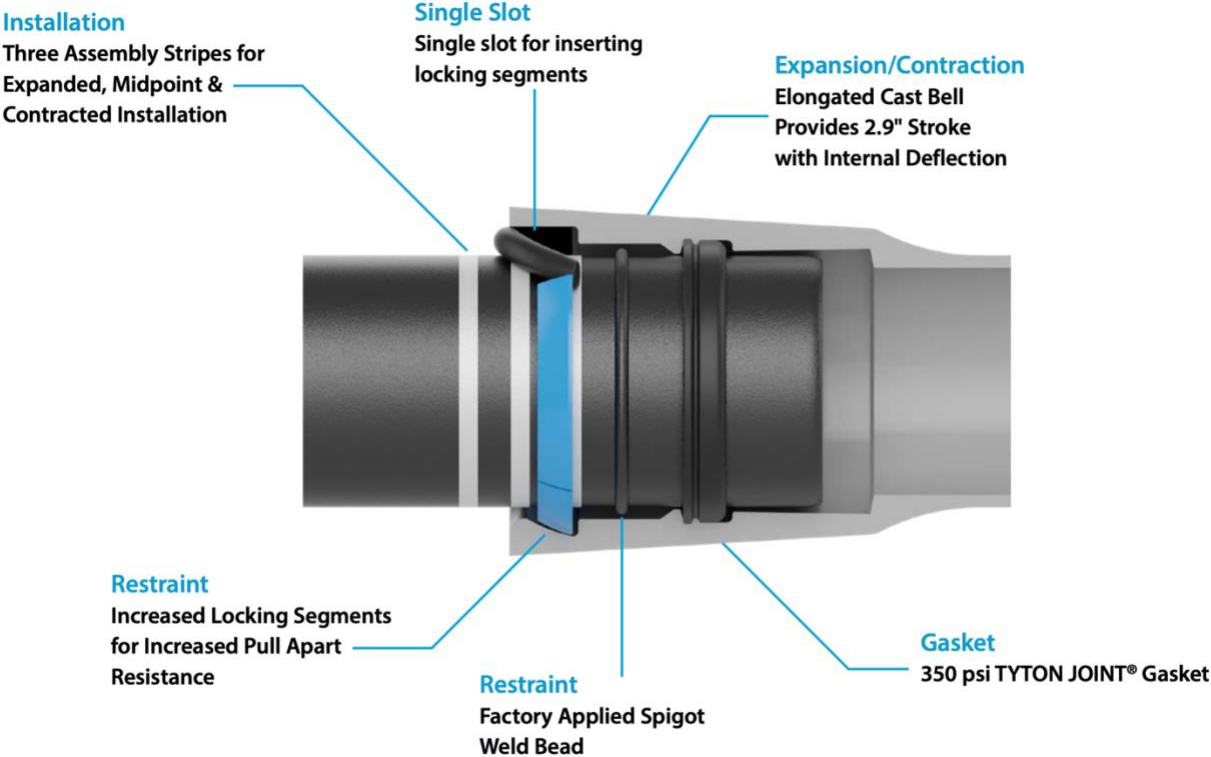
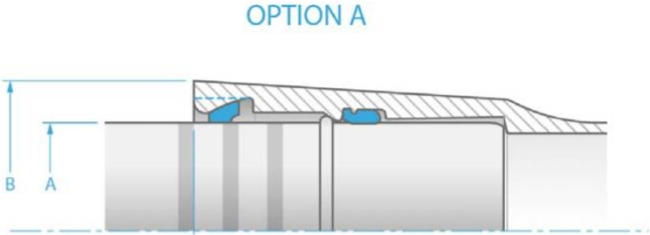
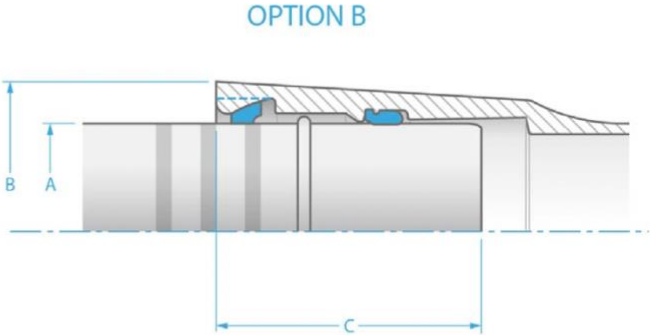


Figure 1-1 Schematic drawing of TR-XTREME™ joint (U.S. Pipe, 2020)

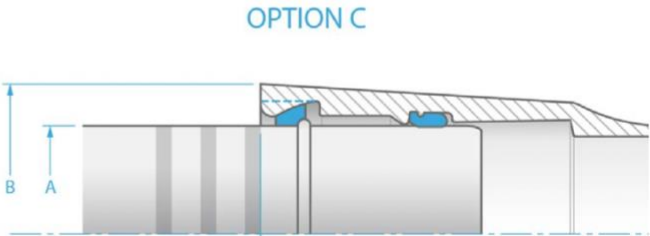
**Option A-Collapsed** – Correct assembly is determined when the front edge of the assembly stripe furthest from the spigot tip lines up with the face of the pipe bell as viewed from above, leaving only one assembly stripe shown.



**Option B-Midpoint** – Correct assembly is determined when the front edge of the middle assembly stripe lines up with the face of the pipe bell as viewed from above, leaving two assembly stripes shown.



**Option C-Extended (Restrained)** - Correct assembly is determined when the front edge of the assembly stripe closest to the spigot tip lines up with the face of the pipe bell as viewed from above, leaving three assembly stripes shown. This is the proper assembly when immediate joint restraint is required.

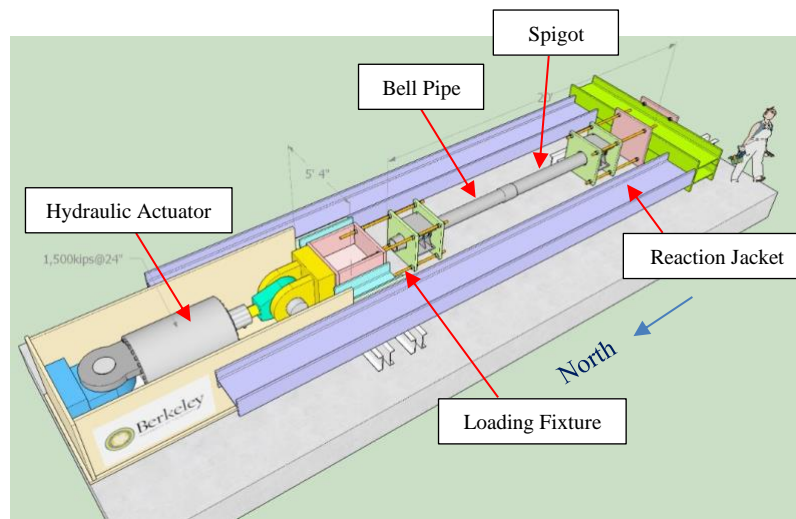


**Figure 1-2 Recommended three installation positions (U.S. Pipe, 2020)**

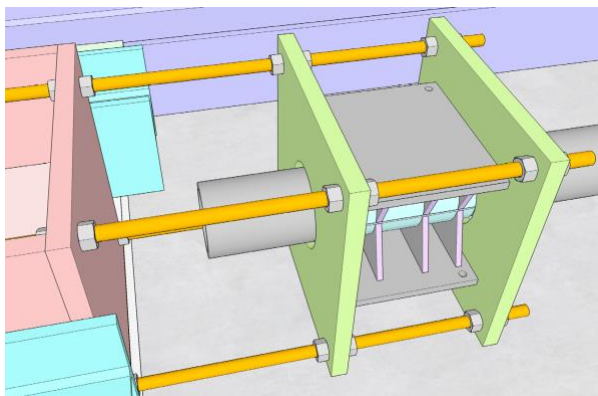
In this study, a finite element (FE) analysis is conducted to simulate the pipe behavior under tension force. This is accomplished by utilizing an elastoplastic material model in ABAQUS (ABAQUS, 2020) and comparing the predicted values with those obtained from the experiments.

## 2 Experimental Setup

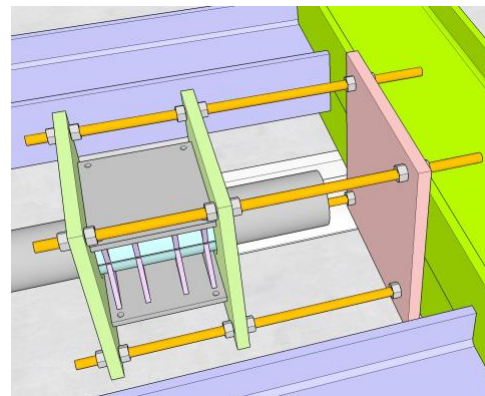
The experimental setup was developed at the Center for Smart Infrastructure (CSI) of UC Berkeley. The sketch of the entire setup is shown in Figure 2-1. The overview of the fully assembled setup of the direct pipe tension test is shown in Figure 2-2. A self-reacting frame was designed to accommodate the loading and reaction sections. A hydraulic actuator with a capacity of 700 kips in tension and 940 kips in compression with a total stroke of 12 inches was utilized in this experiment. Two special jackets were designed and manufactured to restrain the pipeline, as shown in Figures 2-1(b) and (c). The hydraulic actuator transferred the force to the bell pipe via the loading fixture bearing with the weld bead at the end of the pipe. A similar mechanism was used to connect the spigot to the reaction beam.



(a) Setup of the experiment

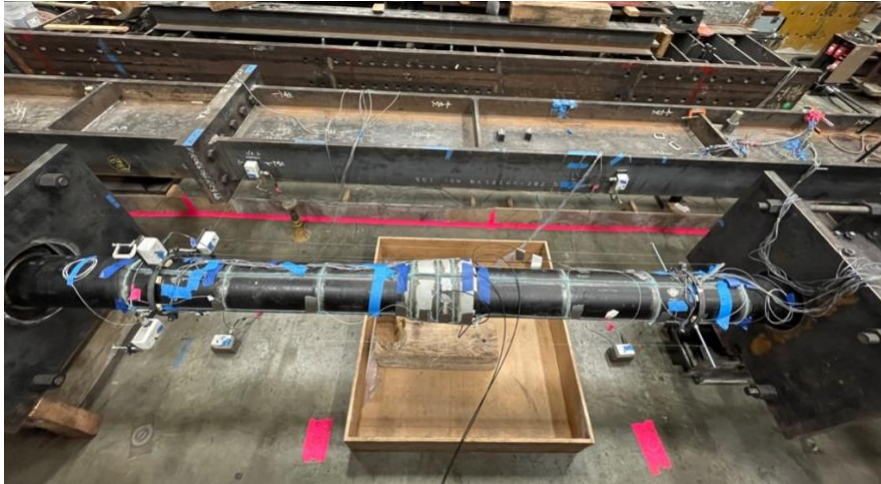


(b) Setup of connection at the loading side



(c) Setup of connection at the reaction side

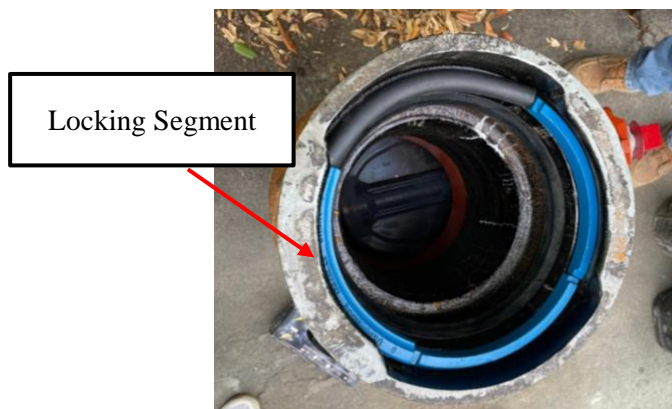
Figure 2-1 Experiment setup



**Figure 2-2 Overview of experiment setup**

The pipe used in the experiment was manufactured by US Pipe, part number TR-XTREME™ with a nominal diameter of 8 inches, and it was made of ductile iron. The manufacturer specifies three assembly positions for installing the bell and spigot: collapsed, midpoint, and extended. For the first experiment, the spigot was fully inserted into the bell (i.e., the collapsed position), meaning that two assembly stripes were inserted into the bell, with the remaining one stripe outside the bell that is visible. When inserted at the collapsed position, the setup provides 2.9 inches strokes for total travel along the pipe's axis. On the other hand, midpoint location was used for the second test, meaning that two assembly stripes were visible and the total travel for the spigot was about 1.5 inches.

Three locking segments were inserted, corresponding to the 3 o'clock, 6 o'clock, and 9 o'clock segments of the bell, as shown by the blue parts in Figure 2-3. A rubber insert was installed at the top of the bell (the 12 o'clock segment) to hold the locking segments in place (the black part in Figure 2-3).



**Figure 2-3 Locking segments and rubber gasket**

# 3 Specimen List and Instrumentation

## 3.1 Test Specimens

Two specimens with different initial and boundary conditions were tested. Both specimens were equipped with a welded feature at the ends of the pipe, which was used as a force transfer mechanism. During the experiment, the welded feature bear against the jacket connected to the actuator to transfer the force from the actuator to the pipe, as shown in Figures 2-1(b) and (c). Specimen 1 was equipped with a single weld bead at the end of the pipe, shown in Figure 3-1(a). On the other hand, the second specimen came with a collar with a double-sided weld (the so-called trust collar), providing a higher capacity for force transfer, as shown in Figure 3-1(b).



(a) End weld bead for Specimen 1



(b) Reinforced end weld bead for Specimen 2

Figure 3-1 Welded features at the ends of the two specimens

Before applying the tension force, the pipes were internally pressurized to 50 psi by water. Specimen 1 was allowed to move in the axial direction while pressurizing. Hence, the spigot slide from the fully inserted condition to the fully extended condition (i.e., three strips are visible) after pressurization. For Specimen 2, the spigot was held in the midpoint location while pressurizing the pipe. By doing so, no relative movement between the pipes occurred during pressurization, and the specimen remained in the midpoint condition at the beginning of the test. The test log is presented in Table 3-1.

Table 3-1 Test log

Test No	Specimen	Test date	End weld bead
1	Specimen 1	4/27/2022	Single weld
2	Specimen 2	7/15/2022	Double-sided weld (trust collar)

### 3.2 Instrumentation

Instrumentation consisted of conventional instruments (strain gauges, position transducers) and distributed fiber optic sensors. The locations of the instruments, observed from four different positions, are shown in Figure 3-2.

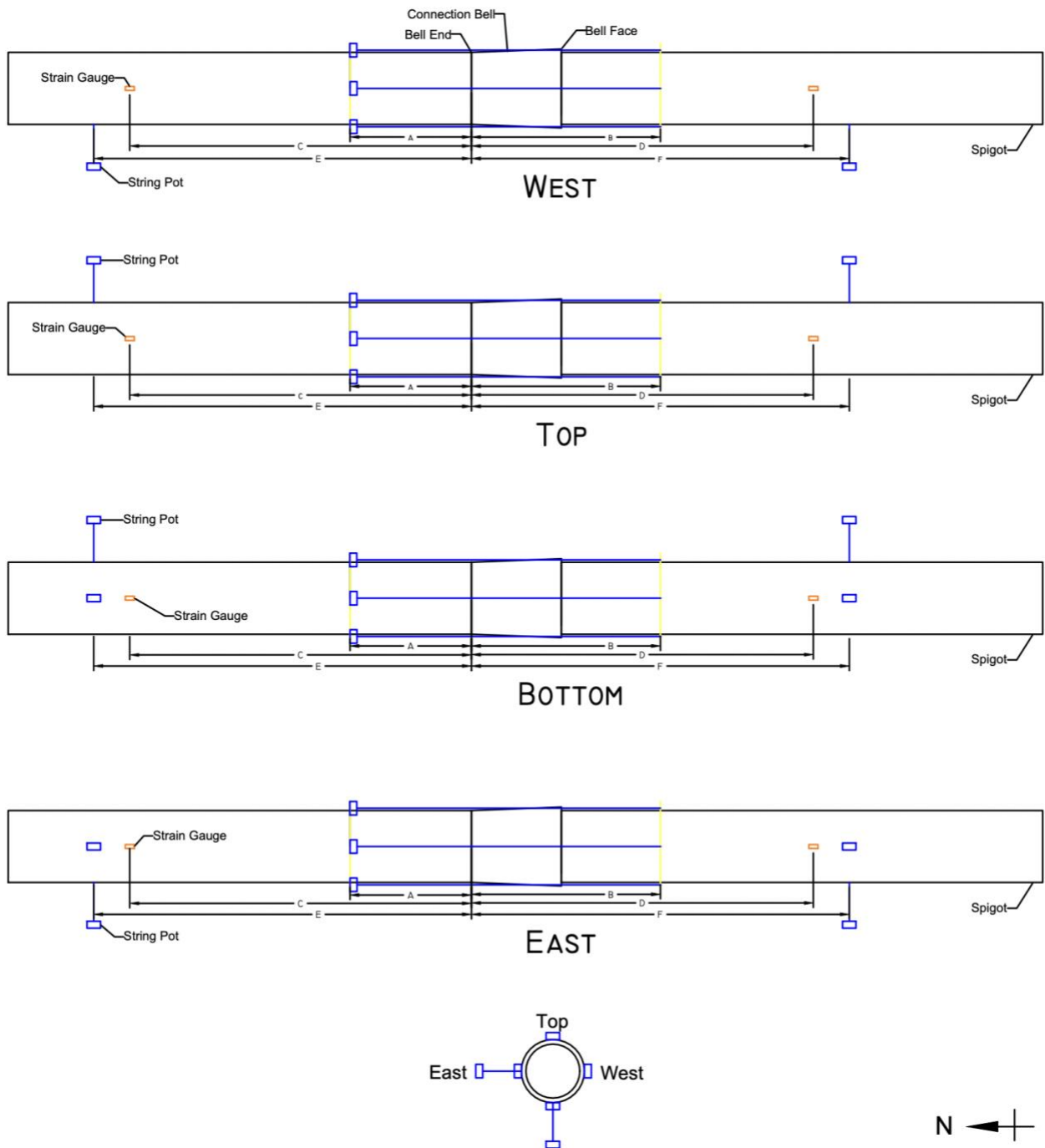


Figure 3-2 Instrumentation plan of conventional instruments

### 3.2.1 Conventional Instruments

Four sets of strain gauges were mounted at the north side of the bell at the position of the top, west, bottom, and east sides (i.e., 3, 6, 9, and 12 o'clock), respectively. Each set of strain gauges includes two strain gauges in the perpendicular directions measuring axial and circumferential strains. Similarly, another four sets of strain gauges were attached to the south side of the bell on the spigot at the same positions. Four position transducers (or string pots herein) were installed at the quarter points around the bell-side pipe circumference and were fixed to the spigot. The string pots were used to measure the joint opening. Another four string pots were used for monitoring displacements of the pipes during the experiment. They were mounted on both ends of the pipes, on the east and bottom sides. The two string pots mounted on the east side aimed to measure the horizontal displacement, and the ones on the bottom side were attached to monitor the vertical displacements. The exact locations of the instruments for the two specimens are listed in Table 3-2. The local instrument names are shown in Table 3-3 for the two specimens.

**Table 3-2 Exact location of the conventional instruments**

	A	B	C	D	E	F
<b>Specimen 1</b>	13.5"	21"	38"	38"	42"	42"
<b>Specimen 2</b>	45.25"	49.75"	42.25"	45.75"	45.25"	49.75"

**Table 3-3 Conventional instrumentation for U.S. Pipe TR-XTREME™ Joint tension test**

Instrument	Location	Specimen 1 - Local Instrument Name	Specimen 2 - Local Instrument Name
String Pot	Parallel to Axial Direction, North of Bell, Top	wp2	wp1
	Parallel to Axial Direction, North of Bell, West	wp3	wp4
	Parallel to Axial Direction, North of Bell, Bottom	wp1	wp3
	Parallel to Axial Direction, North of Bell, East	wp4	wp2
	Perpendicular to Axial Direction, North of Bell, East	wp8	wp6
	Perpendicular to Axial Direction, North of Bell, Bottom	wp6	wp8
	Perpendicular to Axial Direction, South of Bell, East	wp7	wp7
	Perpendicular to Axial Direction, South of Bell, Bottom	wp5	wp5
Strain Gauge	Top of Bell-side Pipe, Axial Strain	B1L	B1L
	West of Bell-side Pipe, Axial Strain	B2L	B4L
	Bottom of Bell-side Pipe, Axial Strain	B4L	B3L

East of Bell-side Pipe, Axial Strain	B3L	B2L
Top of Spigot, Axial Strain	S1L	S1L
West of Spigot, Axial Strain	S2L	S4L
Bottom of Spigot, Axial Strain	S4L	S3L
East of Spigot, Axial Strain	S3L	S2L
Top of Bell-side Pipe, Circumferential Strain	B1R	B1R
West of Bell-side Pipe, Circumferential Strain	B2R	B4R
Bottom of Bell-side Pipe, Circumferential Strain	B4R	B3R
East of Bell-side Pipe, Circumferential Strain	B3R	B2R
Top of Spigot, Circumferential Strain	S1R	S1R
West of Spigot, Circumferential Strain	S2R	S4R
Bottom of Spigot, Circumferential Strain	S4R	S3R
East of Spigot, Circumferential Strain	S3R	S2R


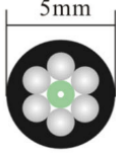
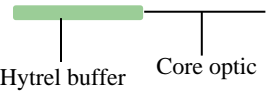
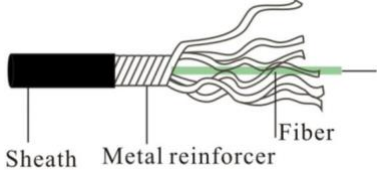


### 3.2.2 Fiber Optic Sensors

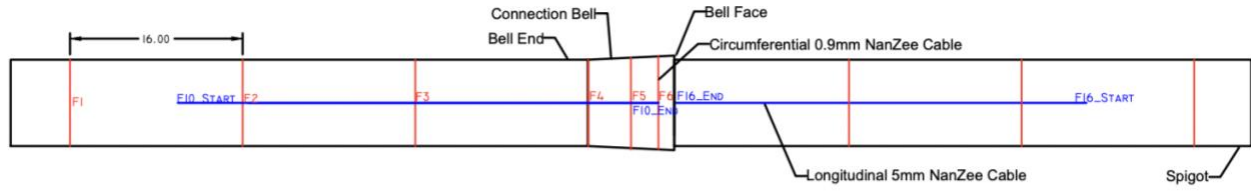
Two types of fiber optic cables manufactured by NanZee Sensing Technology Co. were used; (a) 5 mm diameter armored cable (NanZee 5mm) and (b) 0.9 mm diameter cable (NanZee 0.9mm). Table 3-4 lists the information of the cables. The difference between the two cables is the thickness and material of the coating. NanZee 5mm cable provides a sheath layer and steel reinforcement, resulting in better protection for the optical core; hence, it can be used for the actual field application. The coating of NanZee 0.9mm cable is thinner than NanZee 5mm cable. NanZee 0.9mm cable has less protection, but a more sensitive strain response is achieved.

Two NanZee 5mm cables and two NanZee 0.9mm cables were used for the experiment and were divided into 17 sensors, numbered F1-F17, via indexing on the cables. The layouts of the cables are shown in Figure 3-3. To mimic the use of construction, NanZee 5mm cables (blue lines) were attached in the longitudinal direction. They were attached on both pipes, 90 degrees apart from each other, numbered F10-F17. To better understand the deformation mechanism of the pipes and connection bell section under pulling conditions, NanZee 0.9mm cables (red lines) were placed in the circumferential direction at different positions of the pipes. They were numbered F1-F9. Three NanZee 0.9mm sensors with about 16 inches of spacing were applied on both pipes. At the connection bell section, two NanZee 0.9mm sensors were attached at the end and middle of the section. Another NanZee 0.9mm sensor was placed on top of the locking segments.

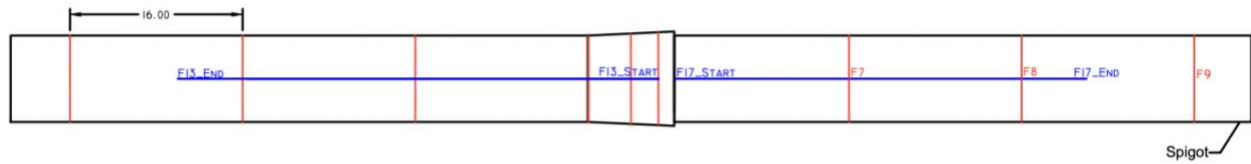
**Table 3-4 Schematic illustration of the selected strain sensor cable (Wu et al., 2015)**

Brand	NanZee Sensing Technology Co.	NanZee Sensing Technology Co.
Model	NZS-DSS-C07	NZS-DSS-C02
Cross section		
Side view		

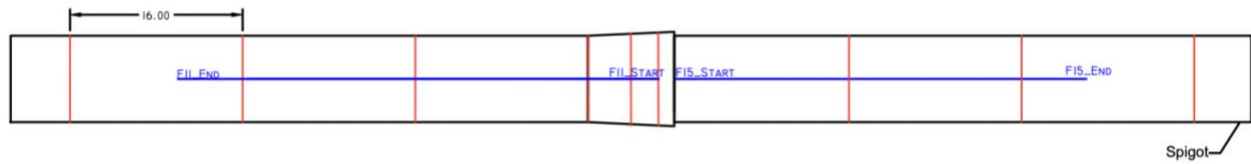
Two types of adhesives were used for the experiment, 3M SCOTCH-WELD DP8010 epoxy and JB-Weld ClearWeld epoxy. Due to the shortage of 3M epoxy, JB-Weld epoxy was used for some longitudinal sections for Specimen 1. The JB-Weld epoxied sections are GN1-EN2 and ES2-GS1. The 3M epoxied sections are EN1-EN2 and ES1-ES2. The corresponding locations are listed in Table 3-7, and visualized in Figure 3-5. For Specimen 2, 3M epoxy was used for all the longitudinal cables. JB-Weld epoxy was used for the NanZee 0.9mm sensors (the circumferential direction) for both of the experiments.



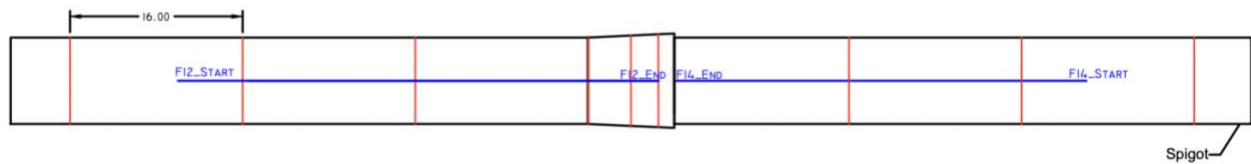
WEST



TOP



BOTTOM



EAST

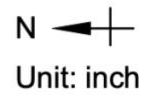
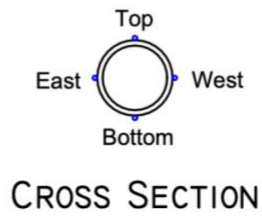
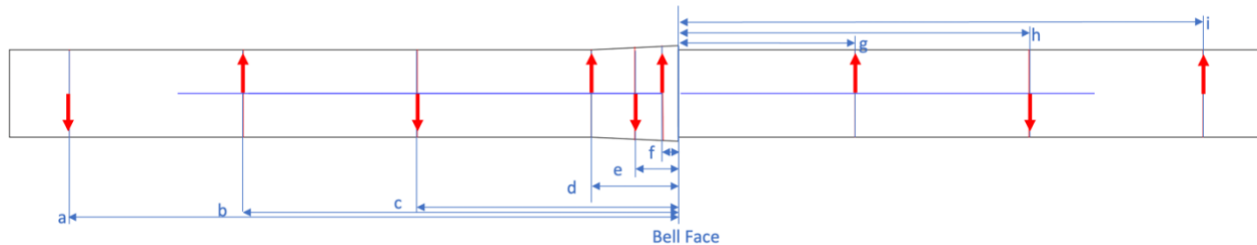


Figure 3-3 Instrumentation plan of fiber optic sensors

**Table 3-5 Fiber optic sensors for U.S. Pipe TR-XTREME™ Joint tension test**

Instrument	Location	Local Instrument Name
Fiber Optic	58.5 inch north of bell face, Circumferential	F1
	42.5 inch north of bell face, Circumferential	F2
	28.5 inch north of bell face, Circumferential	F3
	Bell end, Circumferential	F4
	Mid location of bell, Circumferential	F5
	3.5 inch north of bell face, Circumferential	F6
	16 inch south of bell face, Circumferential	F7
	32 inch south of bell face, Circumferential	F8
	48 inch south of bell face, Circumferential	F9
	Bell pipe, West, Longitudinal	F10
	Bell pipe, Bottom, Longitudinal	F11
	Bell pipe, East, Longitudinal	F12
	Bell pipe, Top, Longitudinal	F13
	Spigot, East, Longitudinal	F14
	Spigot, Bottom, Longitudinal	F15
	Spigot, West, Longitudinal	F16
	Spigot, Top, Longitudinal	F17



**Figure 3-4 Circumferential sensor locations**

**Table 3-6 Exact location of the fiber optic circumferential sensors**

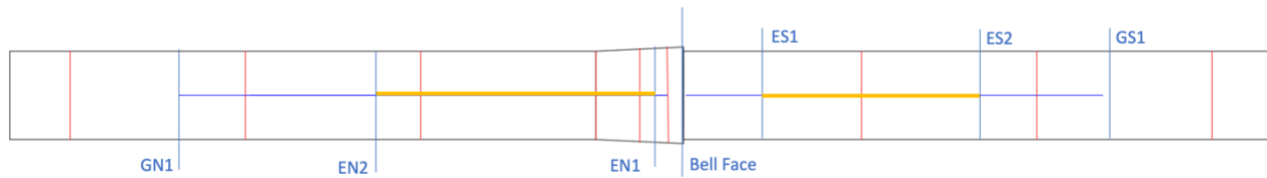
	a	b	c	d	e	f	g	h	i
<b>Specimen 1</b>	59-5/8"	43.5"	27.5"	10.5"	6-7/8"	3.5"	16-5/8"	30-7/8"	45"
<b>Specimen 2</b>	58.5"	42.5"	26.5"	10.5"	6"	3.5"	16"	32"	48"

**Table 3-7 Adhesive location of longitudinal direction cables of Specimen 1**

<b>Specimen 1</b>						
	<b>GN1</b>	<b>EN2</b>	<b>EN1</b>	<b>ES1</b>	<b>ES2</b>	<b>GS1</b>
<b>West</b>	53.75"	24.5"	0	3.5"	27.5"	44"
<b>Top</b>	48.5"	41"	4"	2.5"	27"	41"
<b>East</b>	55"	38.5"	0	5.5"	28"	41.5"
<b>Bottom</b>	66"	58-5/8"	1.5"	4"	28"	43"

<b>Specimen 2</b>						
	<b>GN1</b>	<b>EN2</b>	<b>EN1</b>	<b>ES1</b>	<b>ES2</b>	<b>GS1</b>
<b>West</b>	-	58"	0"	4"	44"	-
<b>Top</b>	-	57"	0"	0"	45"	-
<b>East</b>	-	56"	0"	1.5"	45"	-
<b>Bottom</b>	-	54"	0"	1.5"	41.5"	-



**Figure 3-5 Illustration of adhesive location of cables in the longitudinal direction**

A Rayleigh-based optical frequency domain reflectometry (OFDR), Luna ODiSI 6100 (LUNA, 2022), was used in this experiment. The analyzer is capable of measuring up to 50m long fiber optic cable with an accuracy of less than  $\pm 1$  micro strain when taking a measurement every 0.65mm.

## 4 Test results

All test results are discussed in this section. In addition, a summary of the failure mode and performance of the 8 inches U.S. Pipe TR-XTREME™ joint is included.

### 4.1 Test Data Analysis

The pipes were filled with water and pressurized to 50 psi. A monotonic pull force coinciding with the longitudinal axis of the pipeline was applied. The test was conducted up to the failure of the pipe or a significant water leak.

As mentioned in the previous section, the initial conditions of the two specimens were different. For Specimen 1, the test started directly at the location where the locking segments contact the weld bead. Therefore, no sliding was observed in this test. On the contrary, testing of Specimen 2 started at the midpoint position, which means that several inches of sliding were allowed. The weld bead and the locking segments began to contact each other after around 1.8 inches of sliding. Theoretically, the sliding distance should be around 1.5 inches. The difference is likely due to the installation error of the setup.

Figure 4-1 shows the curves of the average joint opening and load of the two specimens. The peak values of the force are about 188 kips and 174 kips for Specimen 1 and 2, respectively. The maximum load values meet and exceed the minimum pull-apart resistance of 136 kips specified by the manufacturer (U.S. Pipe, 2020). The average joint opening at maximum force is about 0.52 inches (Specimen 1) and 2.46 inches (Specimen 2). Despite the different starting conditions, the peak forces and the displacements reaching the peak force from the start of the loading were similar, indicating repeatability in the results.

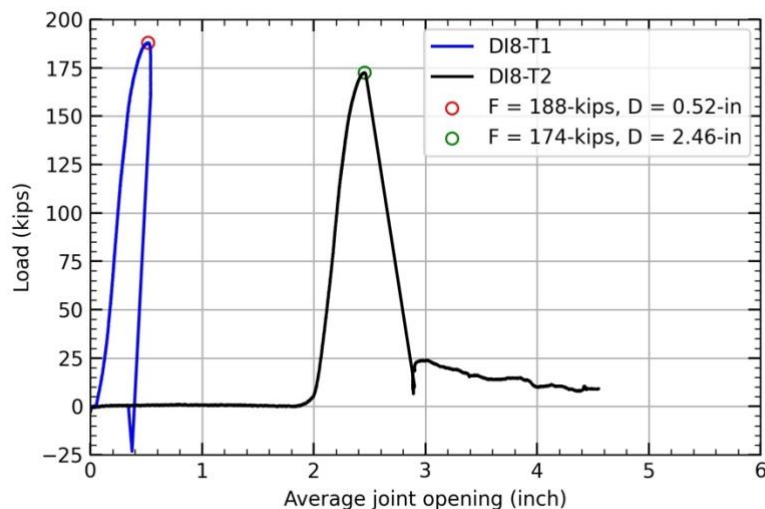


Figure 4-1 Comparison of the tests

### 4.1.1 Axial Strains

As the monotonic force was applied parallel to the pipe's longitudinal direction, the axial strains measured by strain gages were all in tension. Figure 4-2 shows the axial strain vs the axial force of Specimen 1, whereas Figure 4-3 shows that of Specimen 2. For Specimen 1, the maximum axial strain was about  $917 \mu\epsilon$  at the west side of the spigot when the pipe failed. For Specimen 2, the maximum strain is about  $959 \mu\epsilon$  occurred at the top side of the bell pipe. The strains at the east and west sides increased linearly with the applied load. A different strain development pattern can be observed on the top and bottom sides after the force reaches around 120 kips. The tensile strain developed at the top side grows faster than the others. In contrast, the strain on the bottom side drops and grows slower. The non-symmetric placement of locking segments is most likely the reason for this phenomenon. On the top side, instead of having a locking segment, a rubber insert was used to hold the other locking segments in place. The material around the locking segments starts to yield sooner than that on top. Because the locking segments restrained the bottom side of the pipes, the pipe tended to elongate more at the top than at the bottom, so it bowed upwards. As a result, the tension force on top is greater than that at the bottom.

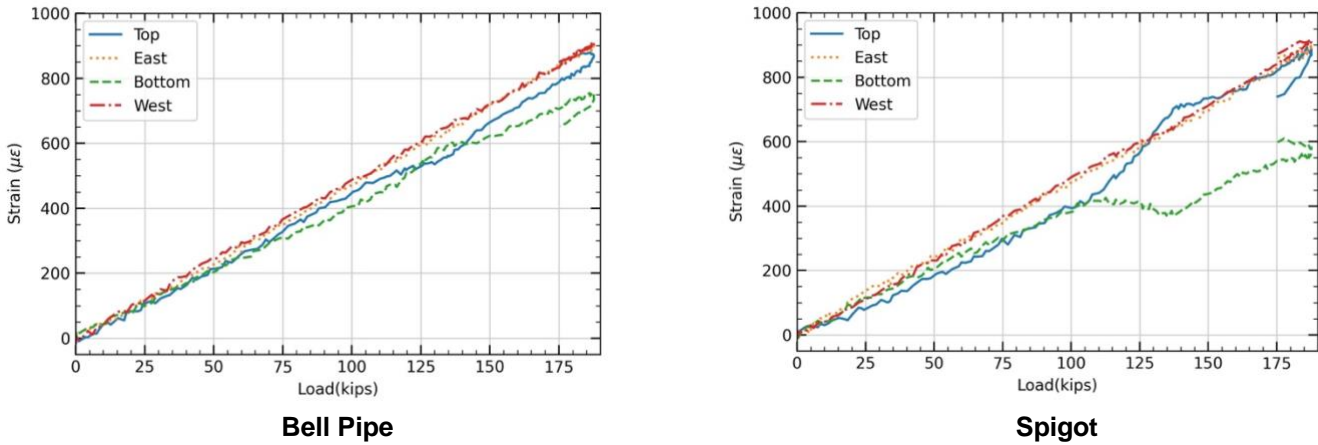


Figure 4-2 Axial strain vs axial force of Specimen 1

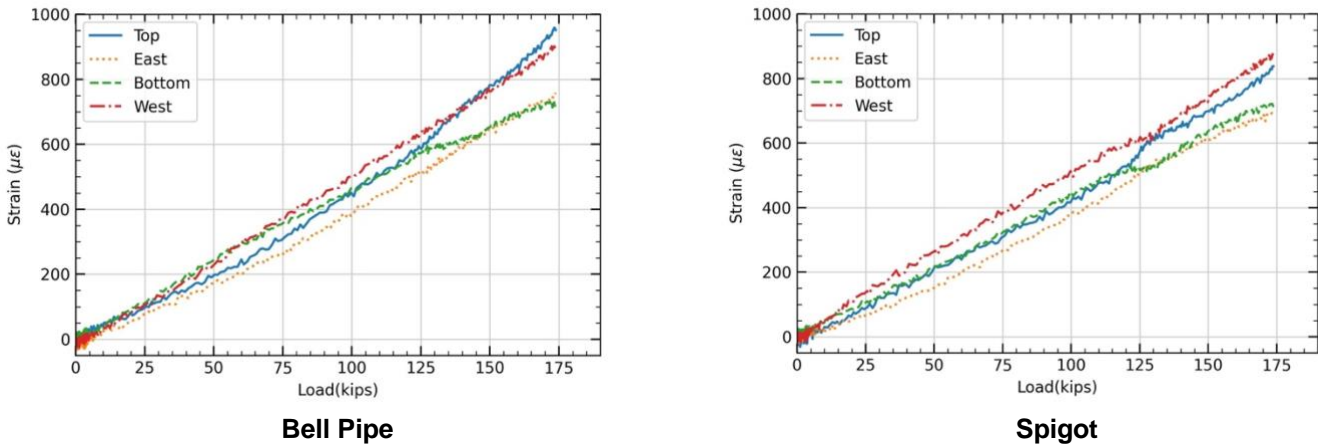
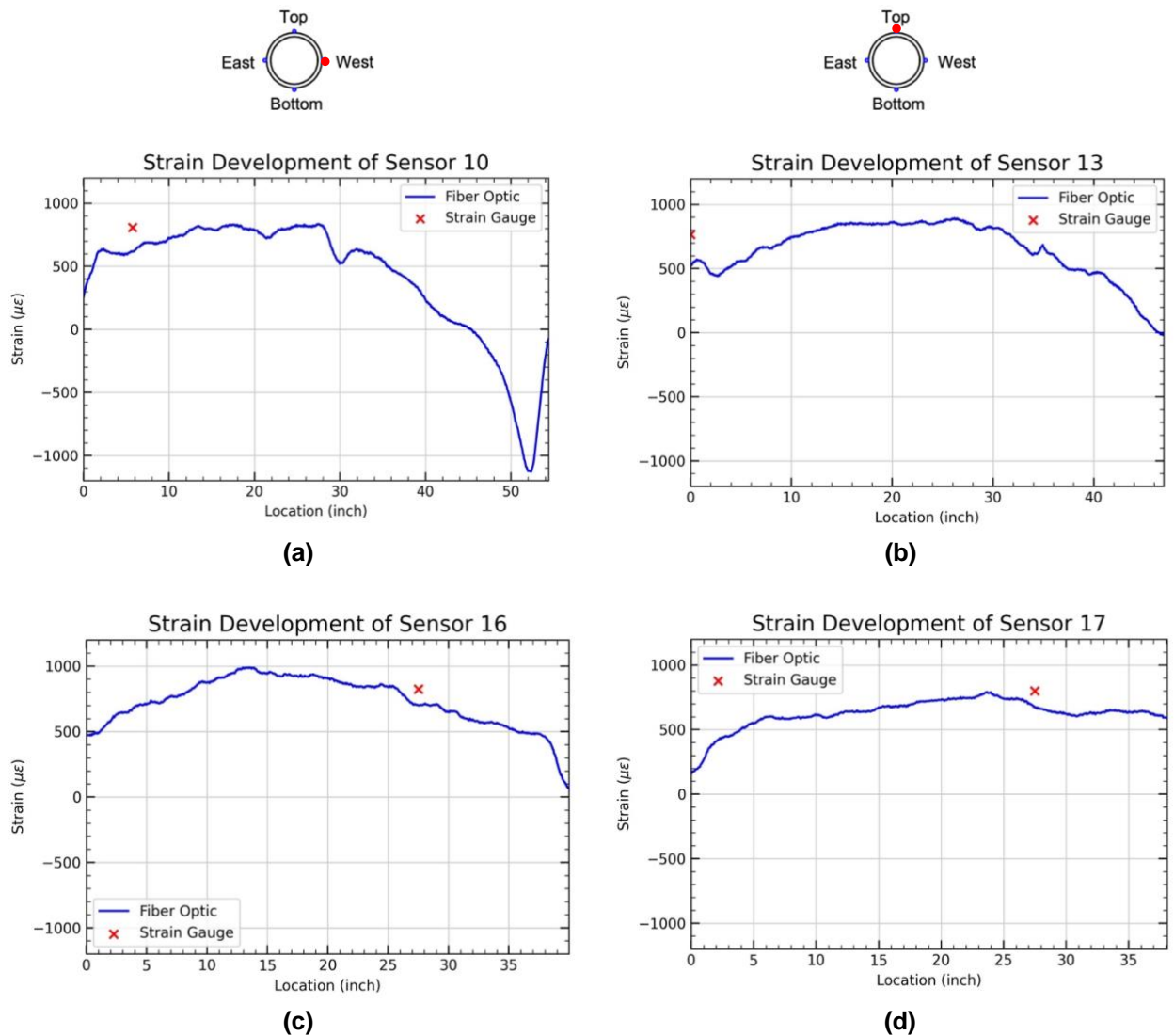
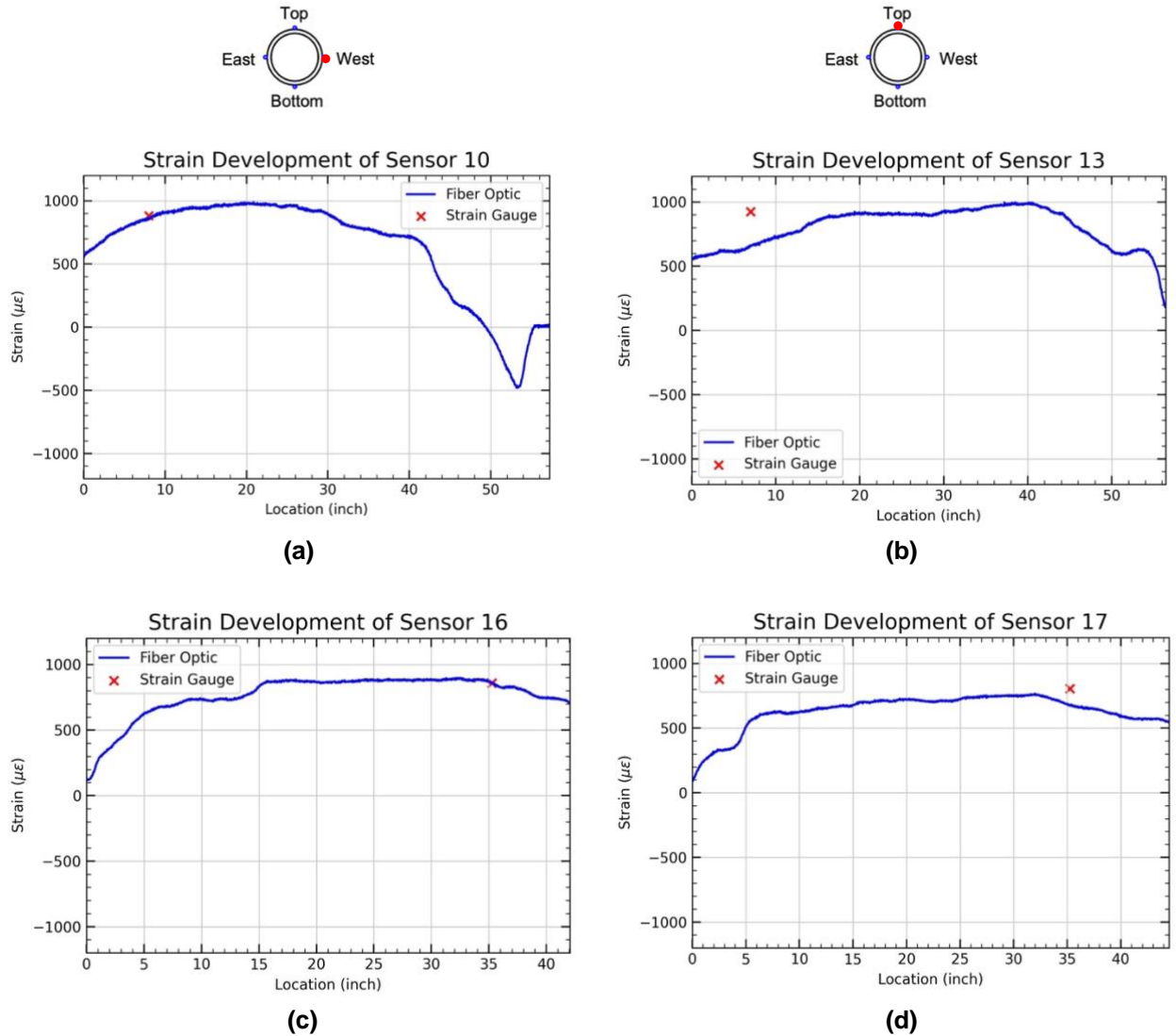


Figure 4-3 Axial strain vs axial force of Specimen 2

Figure 4-4 shows the axial strain distribution under 170-kip force on the west and top sides of the pipes measured by the fiber optic sensors placed on Specimen 1. The strain gauge data are also plotted to show the two data sets are compatible with each other. Sensors 10 and 13 are on the bell side of the pipe; Sensors 16 and 17 are on the spigot. All the strain distribution of the sensors was plotted from the north to the south. Since the pipes were being pulled, most of the sections of the pipes were under tension. However, a large compression section close to the locking segment can be found in Sensor 10. A moment was introduced on the surface as the bell expanded. At the same time, the locking segments were being pulled out, resulting in a significant compression strain on the surface near the locking segment. Since there were about 2.5 inches of cables dispatched close to the bell face on the top and bottom sides, the sensors did not capture this phenomenon on both sides. As a result, this phenomenon can only be found on the west and east sides. Figure 4-5 shows the axial strain distribution results from Specimen 2. Similar to the observation made for Specimen 1, the compression near the locking segment position mentioned above can be found in the west, east, and bottom sides of the bell section.



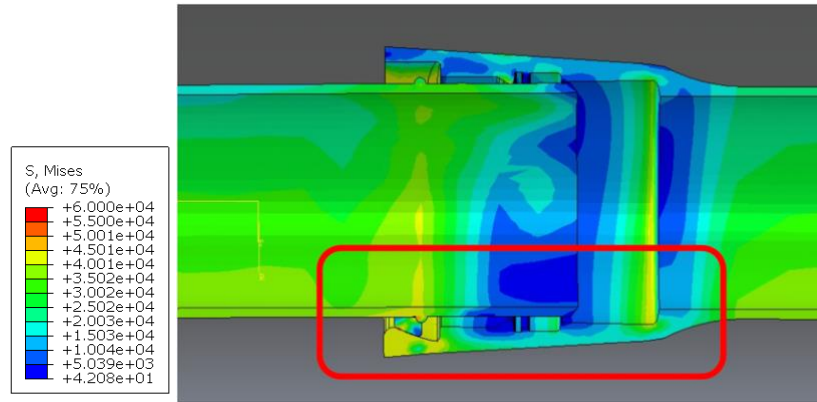
**Figure 4-4 Strain development of Specimens 1 in longitudinal direction under 170-kip loading condition. (a) West side of bell pipe, (b) Top side of bell pipe, (c) West side of spigot, (d) Top side of spigot**



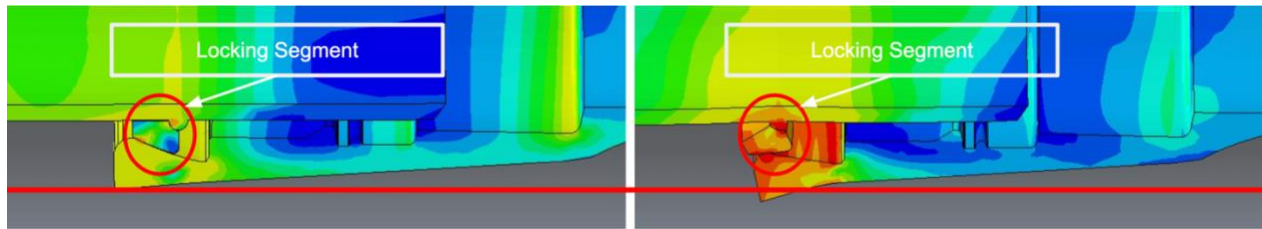
**Figure 4-5 Strain development of Specimen 2 in longitudinal direction under 170-kip loading condition. (a) West side of bell pipe, (b) Top side of bell pipe, (c) West side of spigot, (d) Top side of spigot**

Figure 4-6 sketches the bell failure mechanism from the FE simulations described later. Before the weld bead on the spigot contacts the locking segments, no force is transferred, and the locking segments remain in place without any pipe deformation. However, as the weld bead starts to bear against the locking segments, the locking segments tend to move out, and because of the wedging action, they expand the bell. From the Von Mises stress contours shown in Figure 4-6, it is possible to identify highly stressed areas around the bell, indicating that these areas are more likely to yield and fail. The results of all the fiber optic sensors, including strain versus load and displacement, are given in Appendix A.





(a) Bell sketch



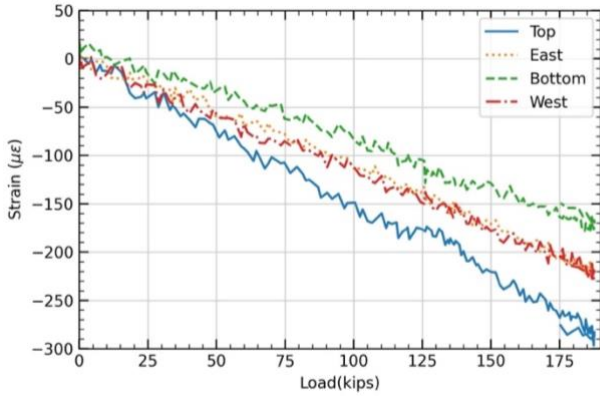
(b) Locking segments start to bear with weld bead

(c) Locking segments being pulled out

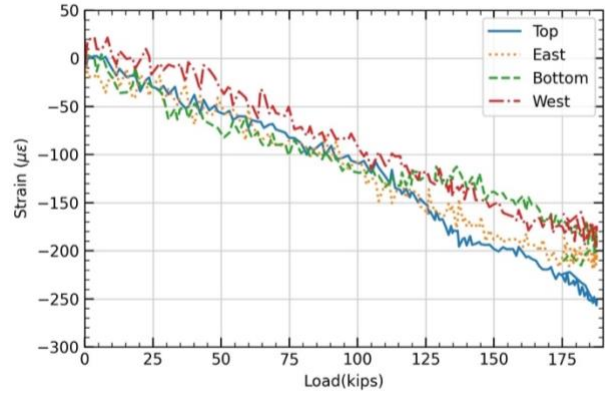
Figure 4-6 Bell failure mechanism

#### 4.1.2 Hoop Strains

The relationships between the hoop strains, measured by strain gauges with actuator axial force, are plotted in Figure 4-7 and Figure 4-8 for Specimens 1 and 2, respectively. Due to Poisson's effect, the strains in the circumferential direction are mainly under compression. For Specimen 1, the minimum hoop strains measured by the strain gages attached to the spigot and bell pipes are about  $-257 \mu\epsilon$  and  $-298 \mu\epsilon$ , respectively. Both of the minimum values occurred on the top side. The magnitude of the hoop strains on the four sides of the spigot is similar. However, the pattern of strain development at the bell-side pipe differs from the spigot side. The magnitude of the strain on the top side is always the greatest, and the one on the bottom side is the smallest. This is related to the non-symmetric placement of the locking segments. For Specimen 2, however, the pattern is not that obvious compared to the observation made in Specimen 1. At failure, the hoop strains measured by the strain gages attached to the spigot and bell pipes are about  $-237 \mu\epsilon$  and  $-216 \mu\epsilon$ , respectively.

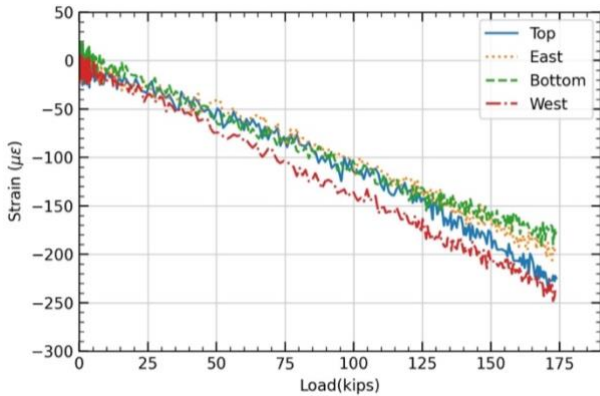


(a) Bell Pipe

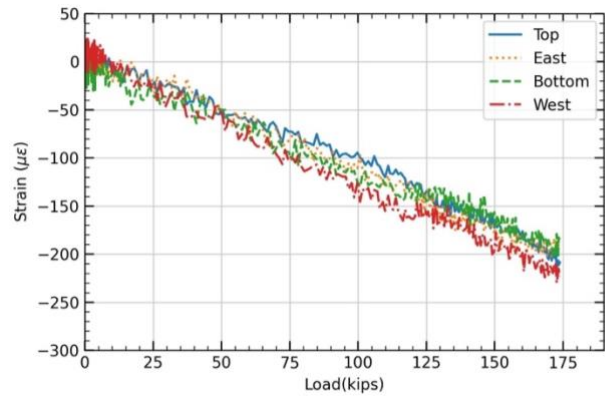


(b) Spigot

Figure 4-7 Hoop strain vs axial force of Specimen 1



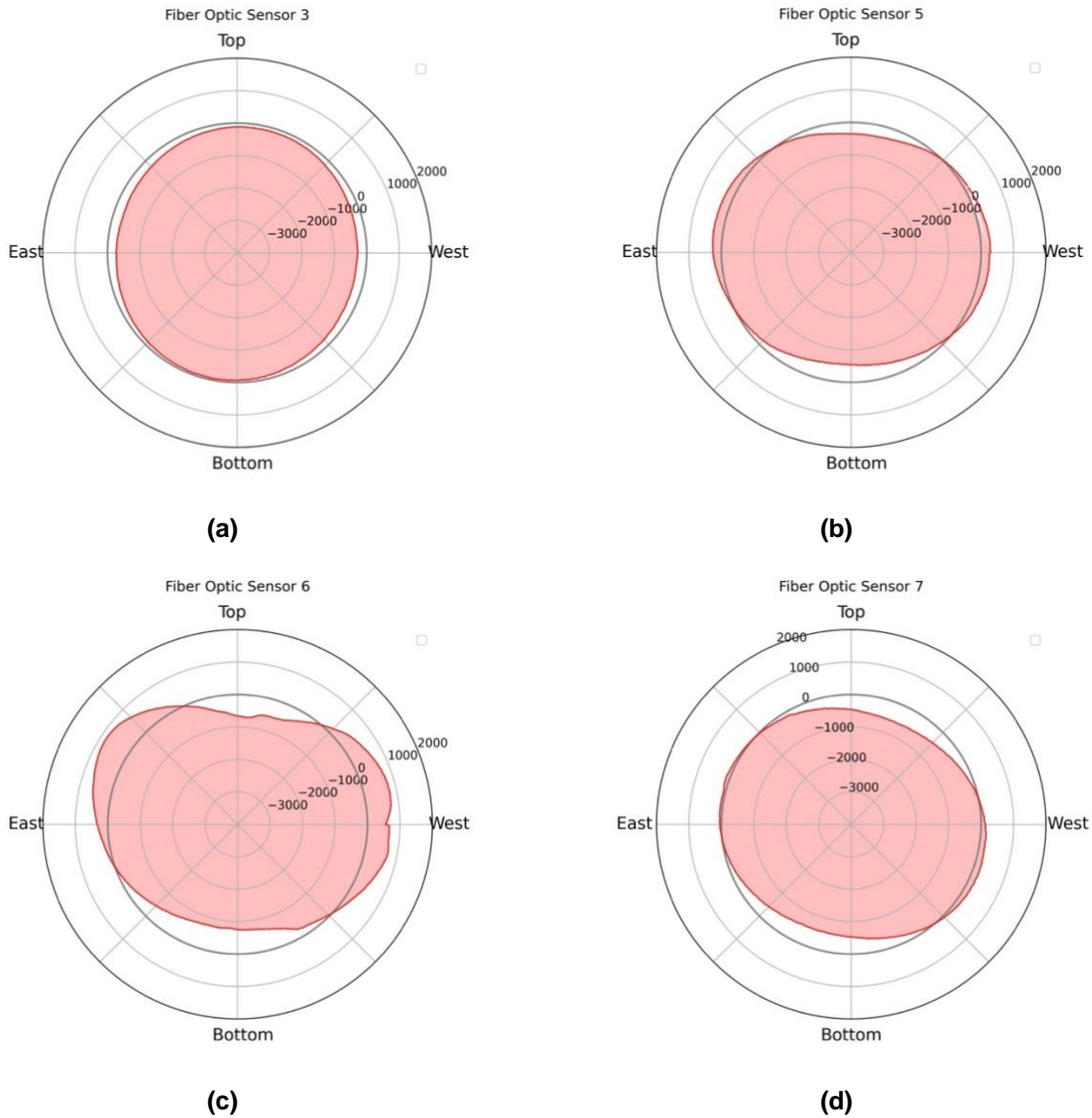
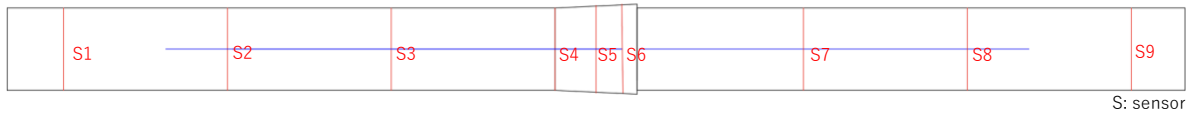
(a) Bell Pipe



(b) Spigot

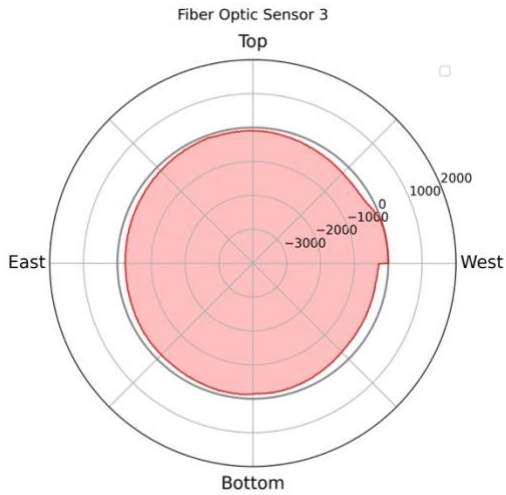
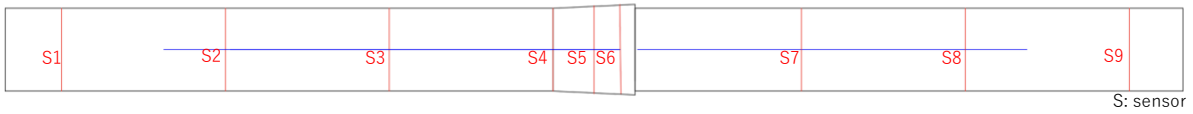
Figure 4-8 Hoop strain vs axial force of Specimen 2

The results of the hoop strain close to the connection bell sections measured by the fiber optic sensors under the 170-kip loading condition in Specimen 1 are plotted in Figure 4-9. The strain distribution pattern of the sensors is similar, indicating that the pipes are squashing. While being pulled, the locking segments in the bell section were in contact with the weld bead on the spigot. Since the top side of the bell was sealed with rubber instead of a locking segment, the bell tends to shrink on the top and bottom sides and expand on the west and east sides, which allows the locking segments to be pulled out. Sensor 6 is close to the locking segments and clearly shows the pattern. The magnitudes of the distributed strains are the largest compared to the other sections. Sensor 5 is the location in the middle of the bell, and the strain is the second largest. Sensors 3 and 7 correspond to the location about 16 inches from the bell. The strains become smaller, indicating the deformation of the pipe is less severe.

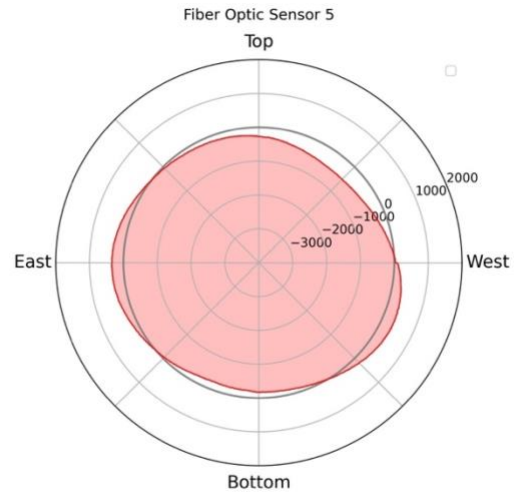


**Figure 4-9 Strain distribution in the circumferential direction under 170-kip loading condition of Specimen 1. (a) sensor on the bell pipe (b) sensor at the mid location of bell (c) sensor on top of the locking segments on the bell (d) sensor on the spigot**

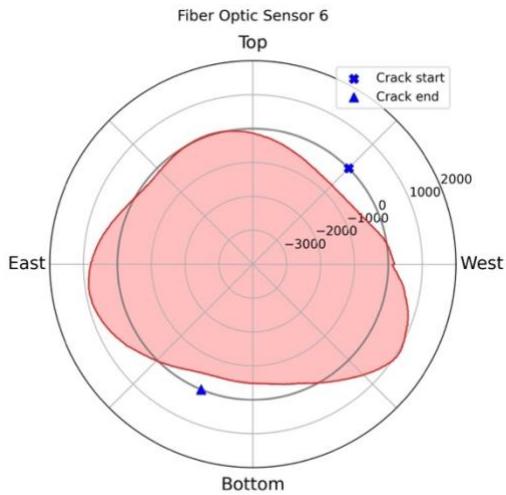
The strain distributions in the circumferential direction measured in Specimen 2 under the 170-kip loading condition are shown in Figure 4-10. The largest compression occurred at around the mid-point of the top and west, which is the first significant crack that occurred. The start and end points of the crack were marked on the plot of Sensor 6. The crack is about 15 inches long, starting from the mid-point of the top and west through the bottom. The strain distribution under different loading conditions was plotted in Appendix A.



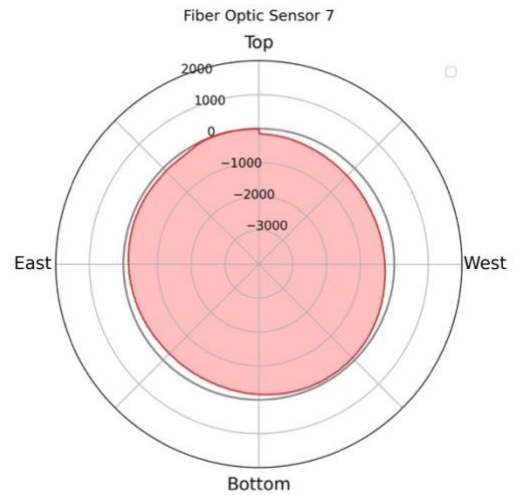
(a)



(b)



(c)



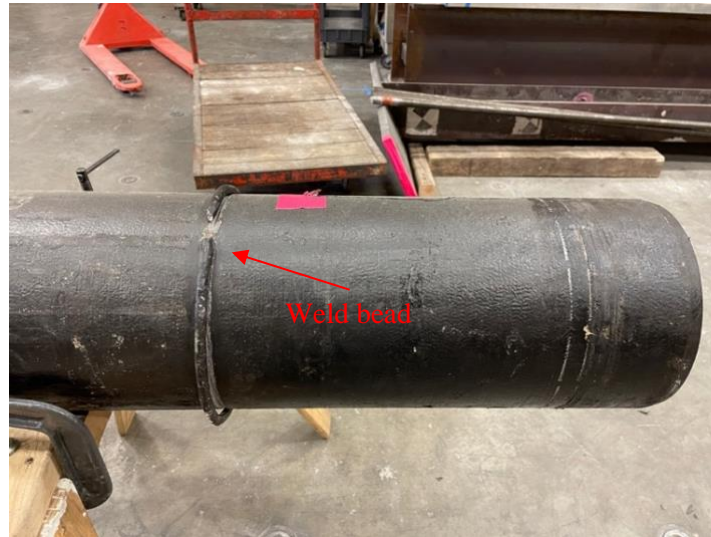
(d)

**Figure 4-10 Strain distribution in circumferential direction under 170-kip loading condition of Specimen 2. (a) sensor on the bell pipe (b) sensor at the mid location of bell (c) sensor on top of the locking segments on the bell (d) sensor on the spigot**

## 4.2 Failure Modes

The experiments were designed to test up to a pipe failure or a significant water leakage resulting in a large water pressure drop. For Specimen 1, the test was stopped due to a failure of the weld bead at the end of the spigot for load-applying purposes, as shown in

Figure 4-11. The weld bead at the end of the pipe was used as a locking mechanism to transfer the force from the spigot to the reaction beam. The weld bead failed in shear at a load of 188 kips without severe damage to the pipe or significant water pressure drop.



**Figure 4-11 Failure of the weld bead at the end of the pipe of Specimen 1**

For Specimen 2, the pipe failed at the bell near the location of the locking segments when the force reached 174-kip with about 2.5 inches average joint opening. As the locking segments were pulled out, a severe crack occurred, starting from the mid-point of the west and top position through the bottom of the bell, as shown in Figure 4-12. At this point, no severe water leakage was observed. The water did not leak until the pipe reached about 4.4 inches of average joint opening, as shown in Figure 4-13. This shows that the pipe possesses the ability to remain functional and continue supplying water even after a severe crack on the bell. The sudden pressure drop shown in Figure 4-13 was a misreading of the water pressure gauge due to the vibration when the bell broke. The results of the two tests are summarized in Table 4-1.



Figure 4-12 Failure of Bell of Specimen 2

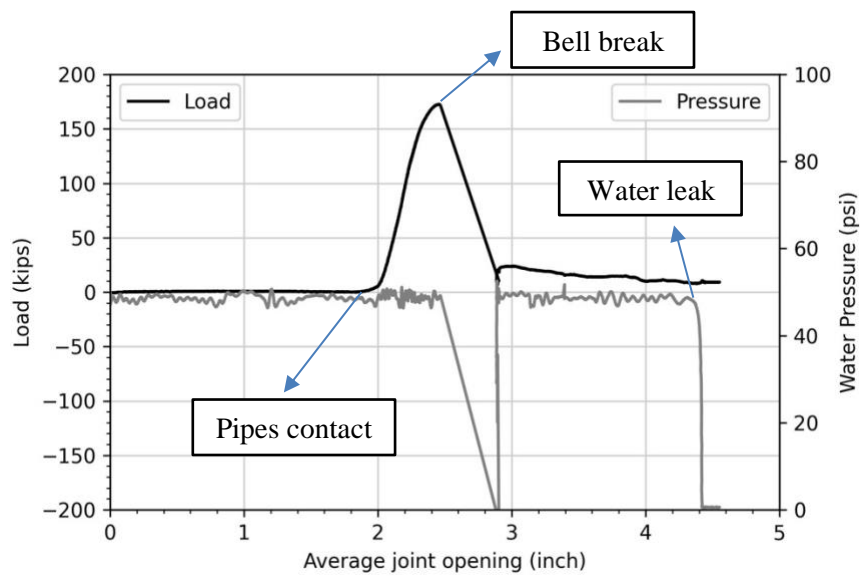


Figure 4-13 Load and water pressure versus average joint opening of Specimen 2

Table 4-1 Summary of the tests

	Max. Load (kips)	Pipe Break Joint Opening (in.)	Water Leakage Joint Opening (in.)	Failed Section
Specimen 1	188	N/A	N/A	Weld bead
Specimen 2	174	2.5	4.4	Bell

# 5 Finite Element Analysis

## 5.1 Overview of Numerical Model

To examine the pipeline behavior due to axial tension force, a 3D full-scale finite element model of the test specimens was developed. ABAQUS, a commercial finite element (FE) modeling software (ABAQUS, 2020), was used to analyze the pipe behaviour under axial tension tests. The geometry of the pipe and joint models were designed to match the experimental setup. The model includes three main parts: a spigot, a bell pipe, and three pieces of locking segments, as shown in Figure 5-1. The FE meshes used for the analysis are shown in Figure 5-2. The mesh density at the bell section was defined to ensure strain development can be accurately determined. The isotropic 3D solid continuum elements (C3D8R) were used to model the pipe and joint. The number of elements and nodes in the finite element model are 124,779 and 157,117, respectively.

The loads and boundary conditions are briefly summarized as follows. At the joint area, the interaction between the pipe and the locking segments is set to be contacted and allowed to slip with respect to each other. The normal behavior of the interaction is set as the hard contact in ABAQUS, and the friction coefficient of the tangential behavior is set as 0.8 according to the standard friction coefficient between materials of ductile iron and steel. The bell end at the fixed box is constrained in all three directions, while the spigot end is allowed to move horizontally. In addition, a 50 psi water pressure was applied to the inner surface of the pipes.

In the model, the initial position of the bell and spigot was located the same as in the experiment of Test 2 (mid-point).

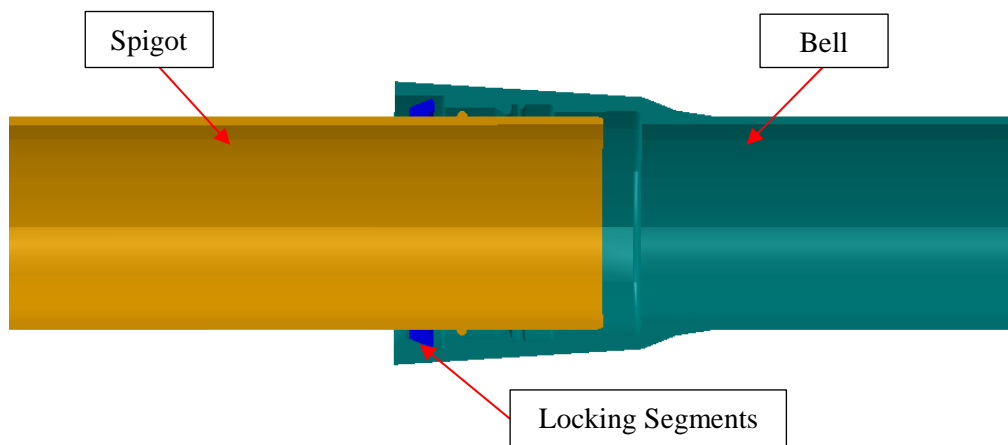


Figure 5-1 Three main parts in the FE model

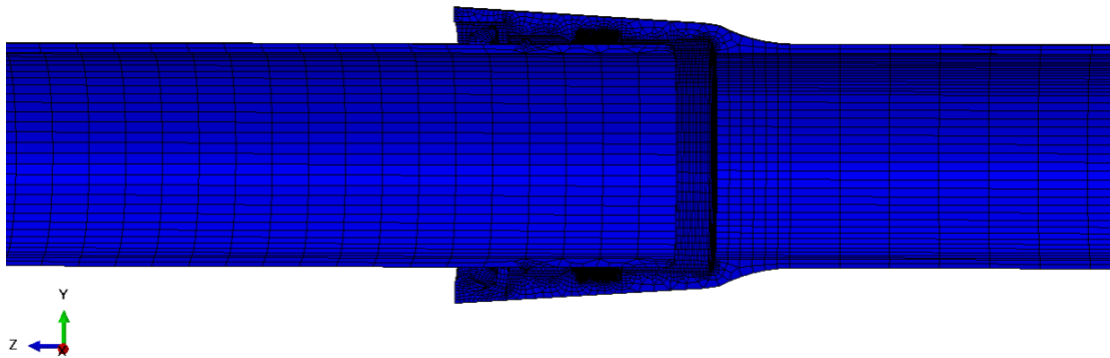


Figure 5-2 3-D FE model mesh for axial tension test

## 5.2 Determination of Pipe Parameters

Table 5-1 presents the material properties provided by the U.S. pipe of the ductile iron pipe and locking segments used in the tests. The plastic properties are included in the simulation to accommodate some parts of the pipe reaching the yielding stress of the material, resulting in plastic deformation status.

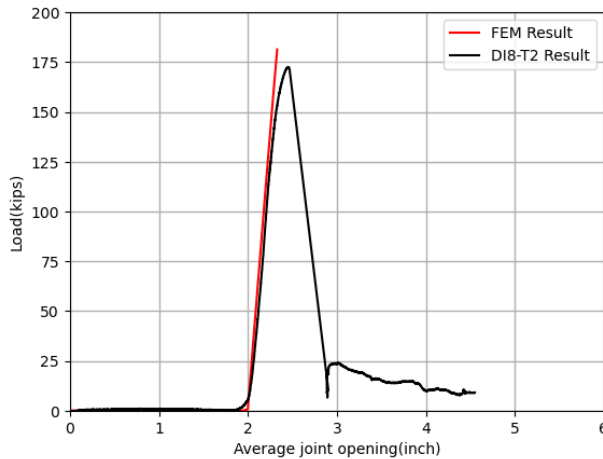
Table 5-1 Ductile iron pipe properties

Part	Density (lb/in <sup>3</sup> )	Young's Modulus (psi)	Poisson's Ratio	Yield Strength (psi)	Ultimate Strength (psi)	Elongation
Ductile Iron Pipe (plastic)	0.28	23,500,000	0.29	42,000	60,000	10%
Locking segments (plastic)	0.3	24,000,000	0.26	42,000	60,000	10%

## 5.3 FEM Results

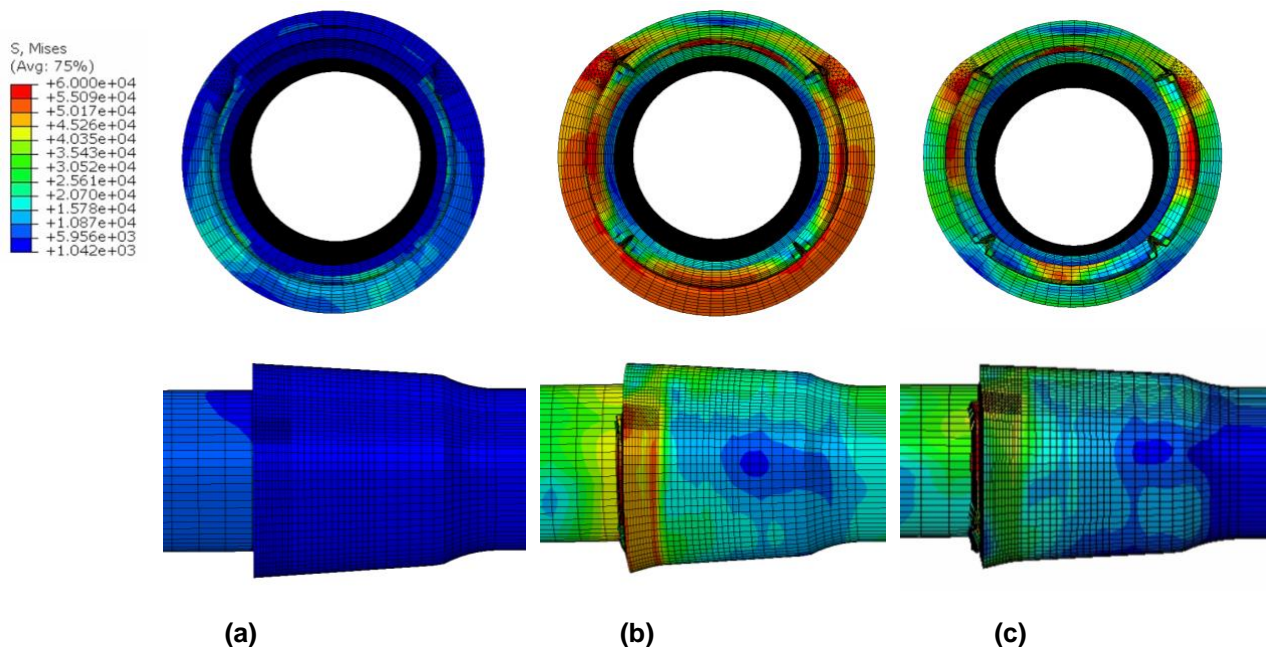
Figure 5-3 shows the comparison of the relationship of the average joint opening and axial force obtained from FE analysis and the experimental result from test 2. The force is very small while the spigot is sliding in the bell. After sliding for about 2 inches, the weld bead and locking segments contact each other and hence the axial force started to develop.





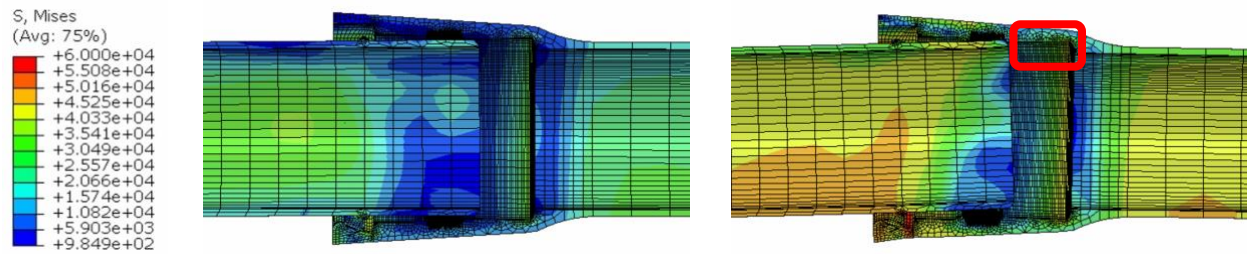
**Figure 5-3 Comparison of FEM result and experimental result of test 2**

Figure 5-4 shows the stress contours and deformation of the joints when the actuator displacement reaches 2 inches, 2.4 inches and 2.9 inches, respectively. The figure shows the bell gradually expands as the locking segments are being pulled out. When the displacement reaches 2.4 inches, the stress reaches the maximum value, resulting in the bell section squashing and decreased thickness in the cross-sectional plane, likely to be the mode of deformation governing failure. Then, the locking segments are pulled out as shown in Figure 5-4(c), which is associated with water leakage observed when pullout to around 2.9 inches in the experiments.



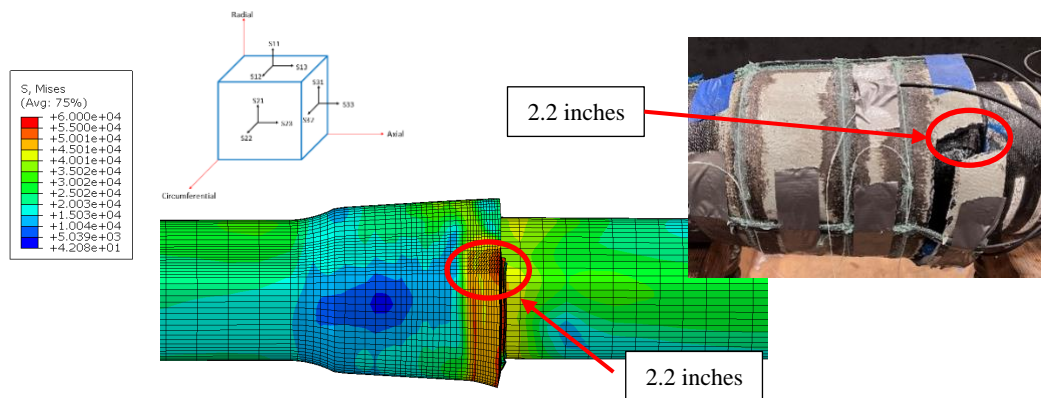
**Figure 5-4 The stress contours of deformed joint at applied: (a) displacement=2 inches; (b) displacement=2.4 inches; (c) displacement=2.9 inches;**

The numerical results are consistent with the experimental observation that the joint tends to move upwards after locking segments contacted the weld bead, as shown in Figure 5-5. Joint rotation occurs due to loss of contact stress between the top side of the spigot and bell gasket.



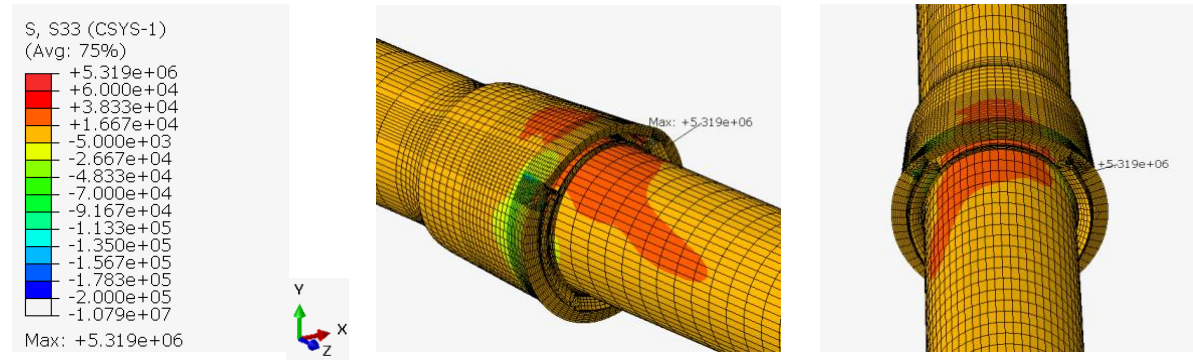
**Figure 5-5 Sectional view of joint rotation**

Figure 5-6 shows the FEM result when the spigot was pulled to 2.4 inches, which corresponds to the loading equivalent to 170 kips (close to the maximum loading condition of the lab test). The maximum Mises stress happens at the areas within 2.2 inches from the edge of the bell, matching the failure mode obtained from Specimen 2. Theoretically, the damage to the bell should be symmetric, as shown in Figure 5-4. However, the experimental result shows that the location of the crack starts at 45 degrees from the top and extends through the bottom. However, no crack is observed on the east side of the pipe. The reason may be because of material inhomogeneity.



**Figure 5-6 Damage area comparison**

It can be illustrated that the bell failure is triggered by the combined circumferential stress  $S_{22}$ , axial tensile stress  $S_{33}$ , and shear stress  $S_{23}$ , as shown in Figure 5-7, which is dominated by circumferential and axial tensile stresses. The crack started from the bell edge at the top-west 45-degree area to 2.2 inches; then, the crack propagated to the bottom along the circumferential direction, as shown in Figure 5-6.

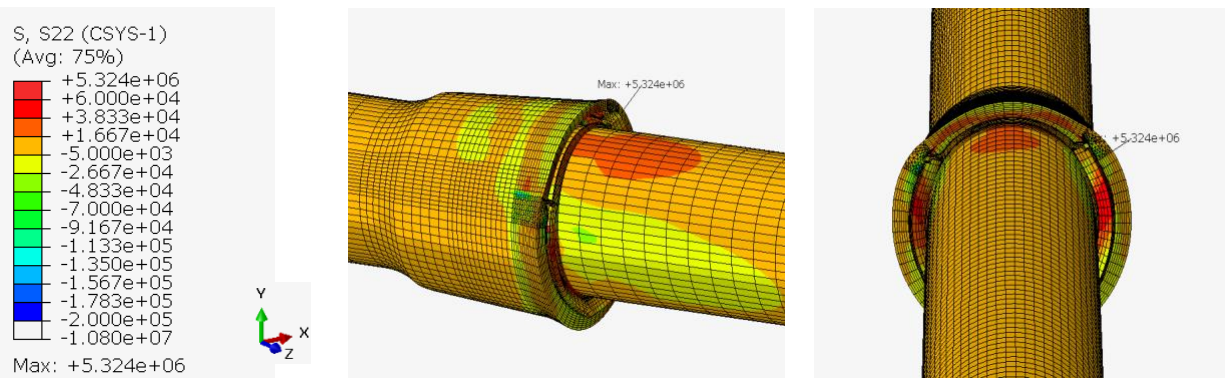


Cylindrical coordinates

Axial tensile stress S33

Axial tensile stress S33

(a)

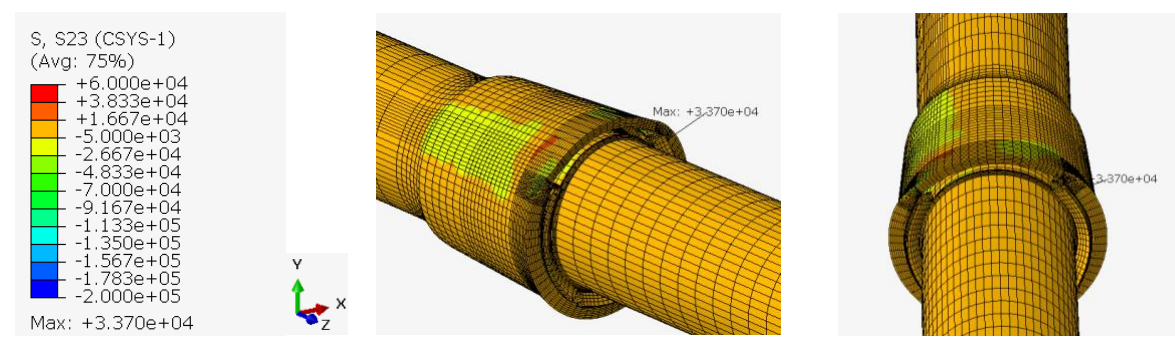


Cylindrical coordinates

Circumferential stress S22

Circumferential stress S22

(b)



Cylindrical coordinates

Shear stress S23

Shear stress S23

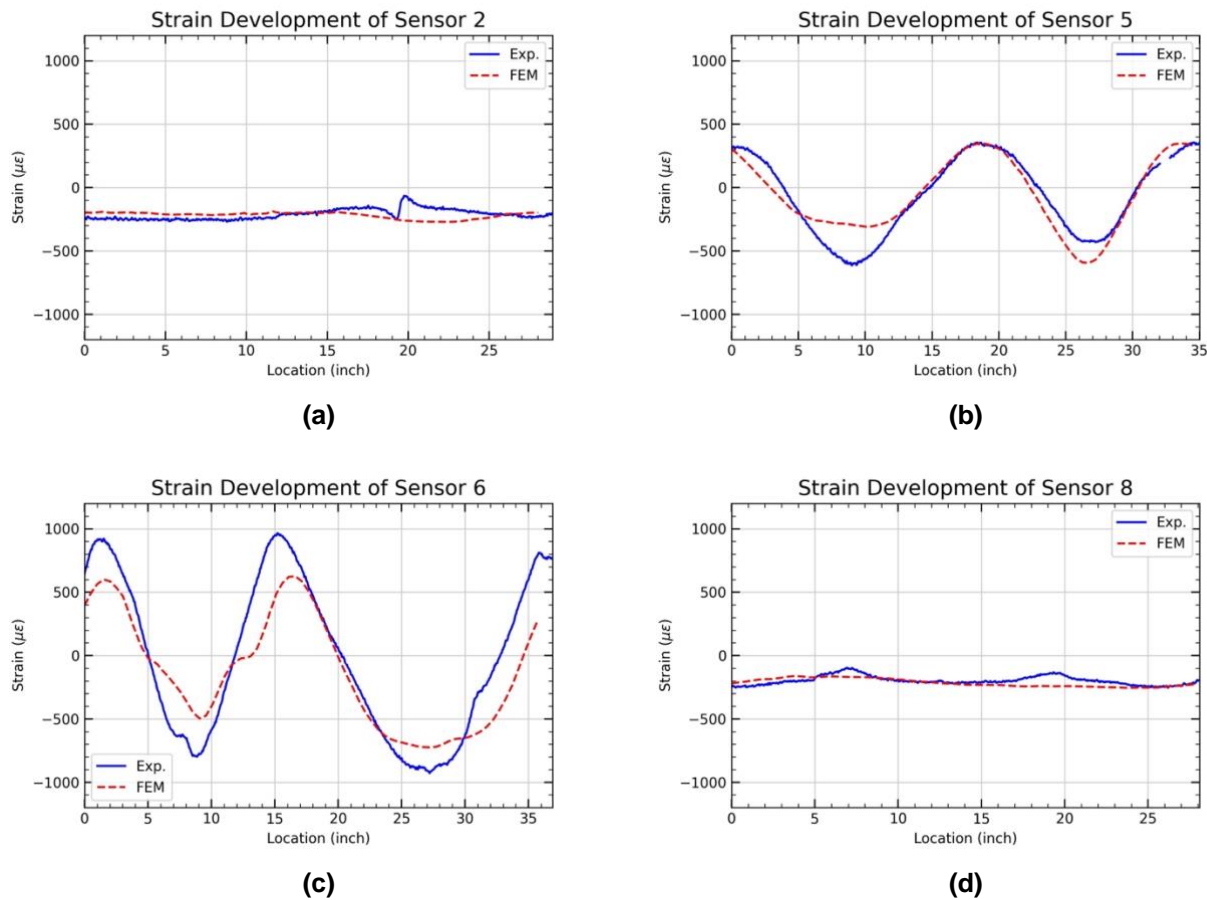
(c)

Figure 5-7 Numerical simulation showing (a) axial tension stress S33; (b) circumferential stress S22 (c) shear stress S23 at 2.4 in. of axial displacement in cylindrical coordinates

### 5.3.1 Comparison of the FE Model and Experimental Data for Specimen 1

Figure 5-8 shows the comparison of the hoop strain distribution from the FE analysis and Specimen 1. Sensor 2 is on the bell pipe, about 32 inches away from the bell end. Sensors 5 and 6 are both on the bell, mid-section of the bell, and locking segment location, respectively. Sensor 8

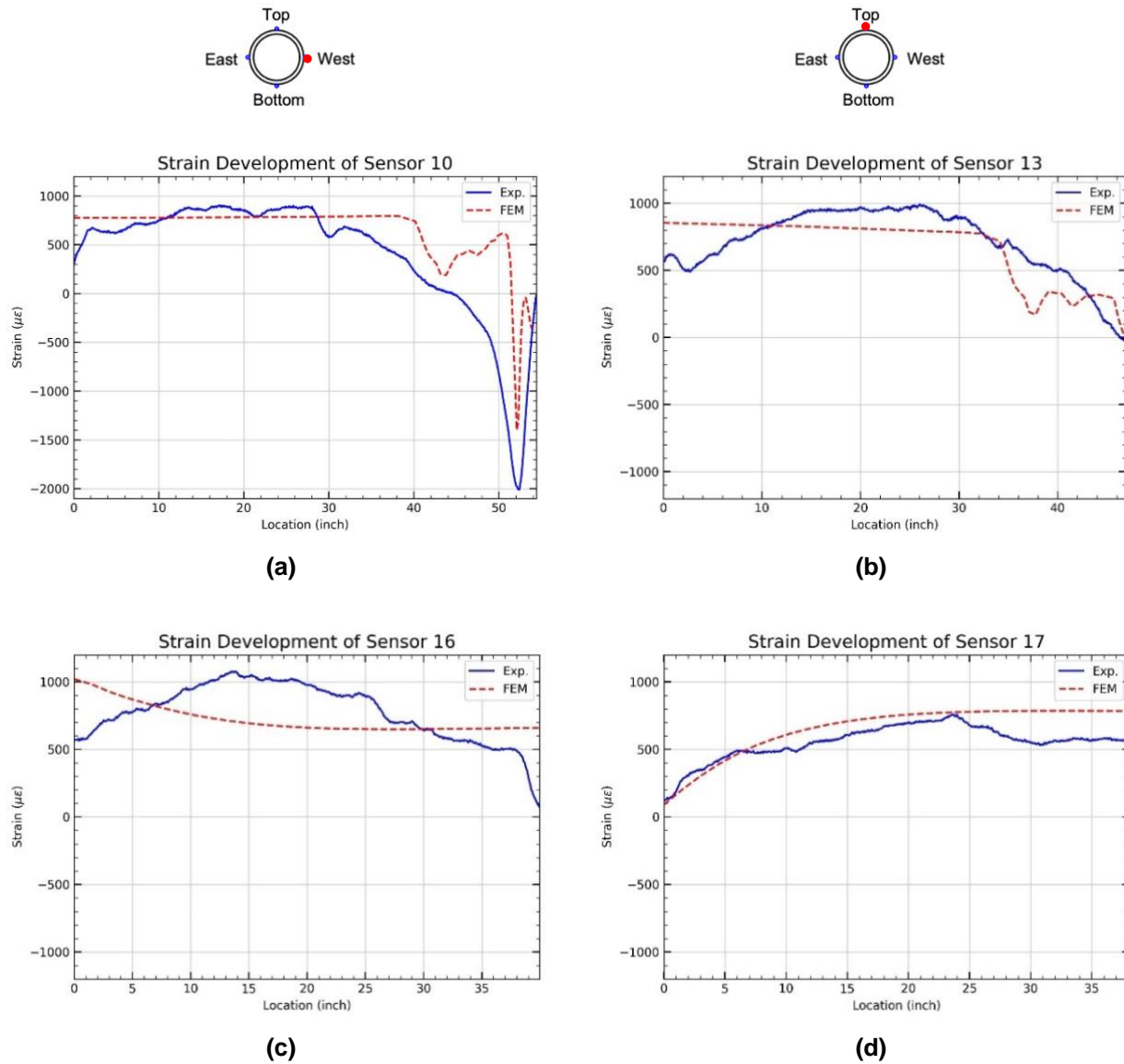
is on the spigot, 32 inches away from the bell face. The patterns of the strain distribution match well between the two data. However, the FE model provides slightly smaller peak strains at the location where Sensor 6 was attached. Numerical simulation simplifies the boundary and loading conditions. In the FE model, the boundary conditions were simplified as follows; (1) the bell end was set as a fix end (i.e., no movement and moment were allowed in x,y, and z directions), and the spigot end was treated as a roller end (i.e., allowed movement in pipe longitudinal direction). However, for the actual experiment, the perfect fixed boundary condition is hard to achieve. (2) For the bell connection part, the interactions between the pipe and locking segments were set to be normal contact and tangential contact (i.e., neglecting the influence of gravity). (3) For the loading condition, the pure axial tension force was applied on the spigot pipe, which is hard to achieve during the experiment. Despite these differences in the boundary conditions, the results from FE analysis and experiment both agree that the magnitude of the strain observed at the bell section diminishes as the location is further away from the bell, as can be seen from Sensors 2 and 8.



**Figure 5-8 Comparison of hoop strain results from FE simulation and experiment under 185-kip loading condition of test 1. (a) sensor on the bell pipe (b) sensor at the mid location of bell (c) sensor on top of the locking segments on the bell (d) sensor on the spigot**

All the axial strain distributions obtained from the FE simulation were plotted from the north to the south and compared to the experimental data, as shown in Figure 5-9. The results show that the FE model can predict the axial strain distributions. Compared to the experimental result, the FE analysis shows a flatter trend when the locations are away from the bell. On the other hand, at locations close to the bell, the strains vary. This can be clearly observed from Sensor 10 (west side of bell pipe) and Sensor 13 (top side of bell pipe). The results of Sensor 16 (west side of

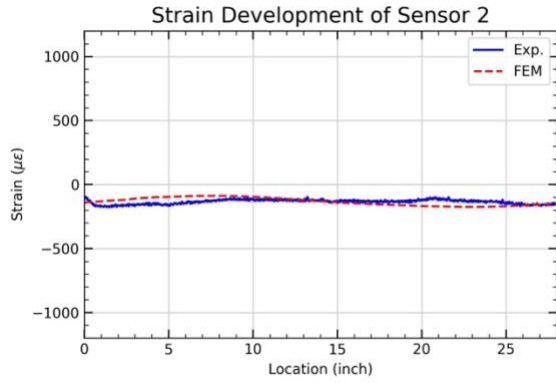
spigot) from the two sources are slightly different. This might be why the FE model does not capture the failure of the weld bead at the end of the pipe. The comparison results of strains between the FE simulation and experiment are given in Appendix B.



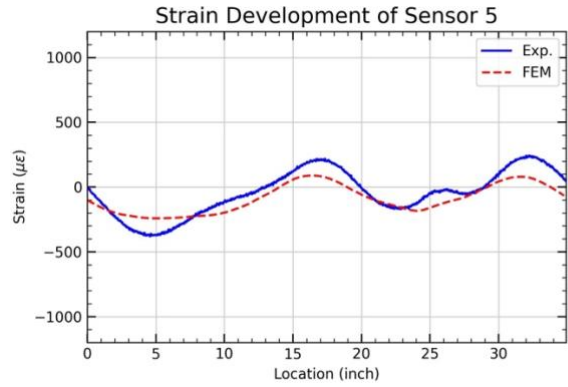
**Figure 5-9 Comparison of axial strain results from FE simulation and experiment under 185-kip loading condition of test 1. (a) West side of bell pipe, (b) Top side of bell pipe, (c) West side of spigot, (d) Top side of spigot**

### 5.3.2 Comparison of the FE Model and Experimental Data for Specimen 2

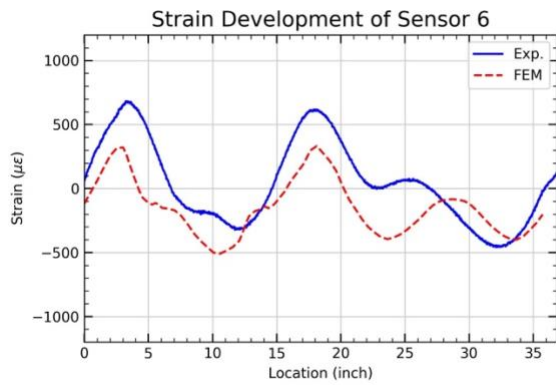
Figure 5-10 and Figure 5-11 show a good agreement between the FE result and specimen 2 under 125-kip loading condition, indicating that the numerical model was able to simulate the behavior of the pipe under different tensile forces. The boundary and loading conditions of the FE model are similar to the first tension model. The predictive strain at the Sensor 6 location is generally smaller than the actual result, but the pattern remains similar. The reason might be the imperfection of material, or the pipes were not perfectly aligned.



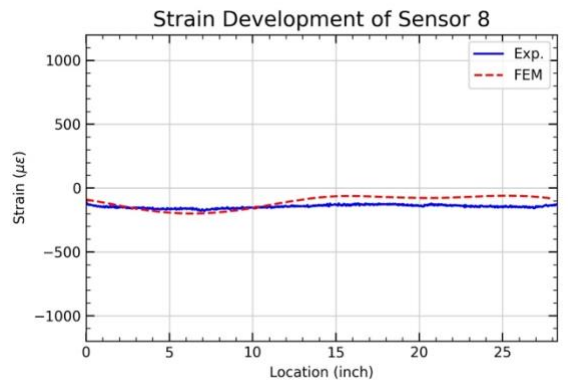
(a)



(b)

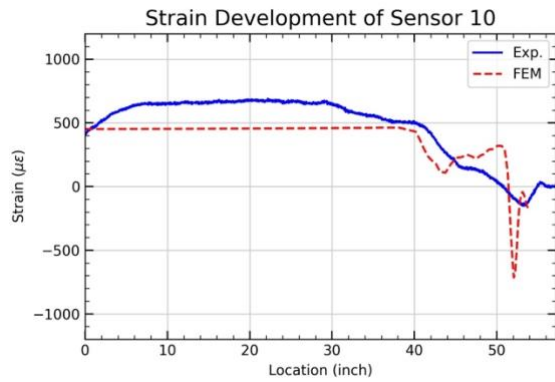
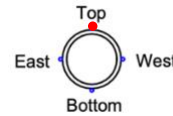
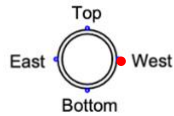


(c)

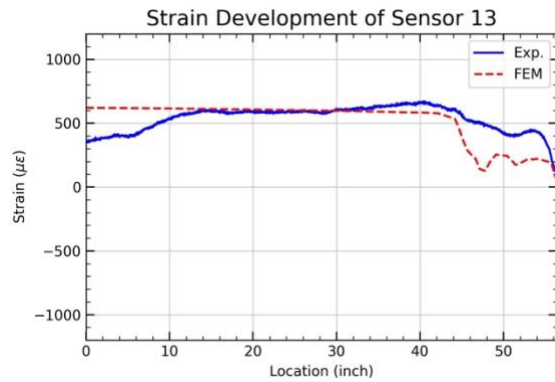


(d)

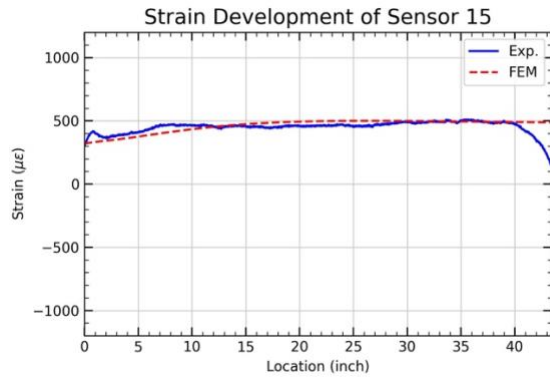
**Figure 5-10 Comparison of axial strain results from FE simulation and experiment under 125-kip loading condition of test 2. (a) sensor on the bell pipe (b) sensor at the mid location of bell (c) sensor on top of the locking segments on the bell (d) sensor on the spigot**



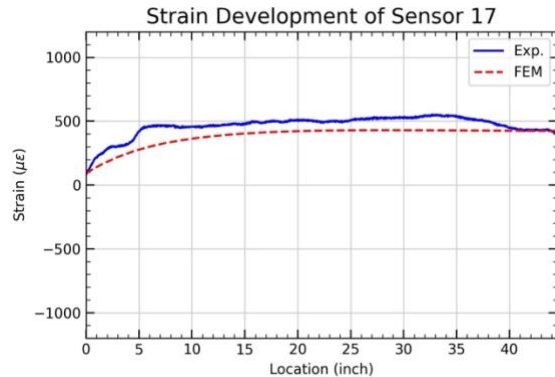
(a)



(b)



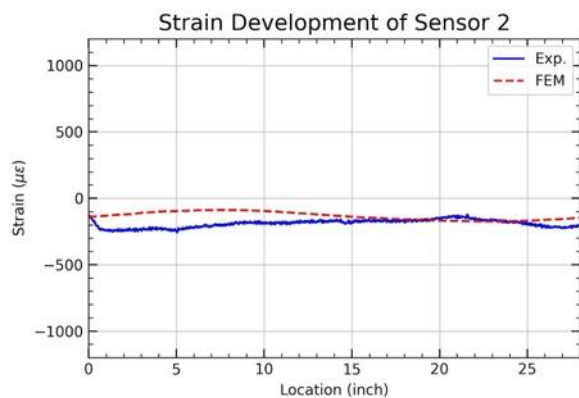
(c)



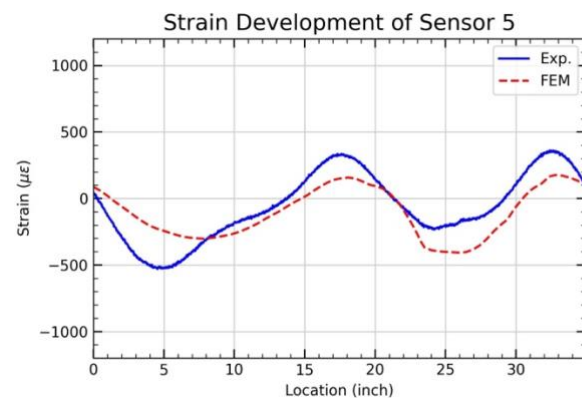
(d)

**Figure 5-11 Comparison of axial strain results from FE simulation and experiment under 125-kip loading condition of test 2. (a) West side of bell pipe, (b) Top side of bell pipe, (c) West side of spigot, (d) Top side of spigot**

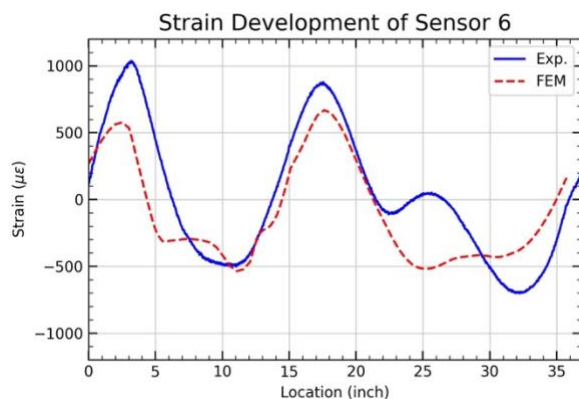
Figure 5-12 and Figure 5-13 show a good agreement between the FE result and experimental data under the 170-kips tensile force condition when the specimen was about to fail. The predicted strain distribution patterns are generally similar to the experimental results. This indicates that the FEM can well predict the strain distribution throughout the pulling process.



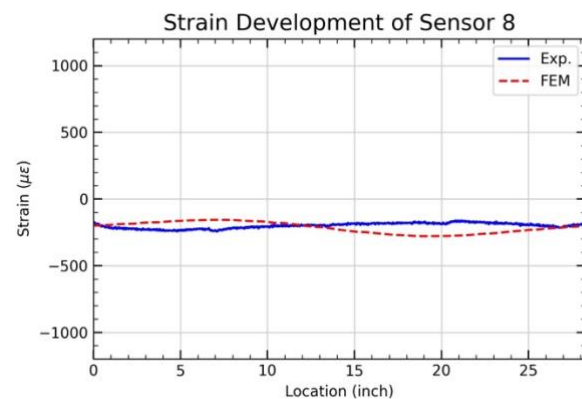
(a)



(b)

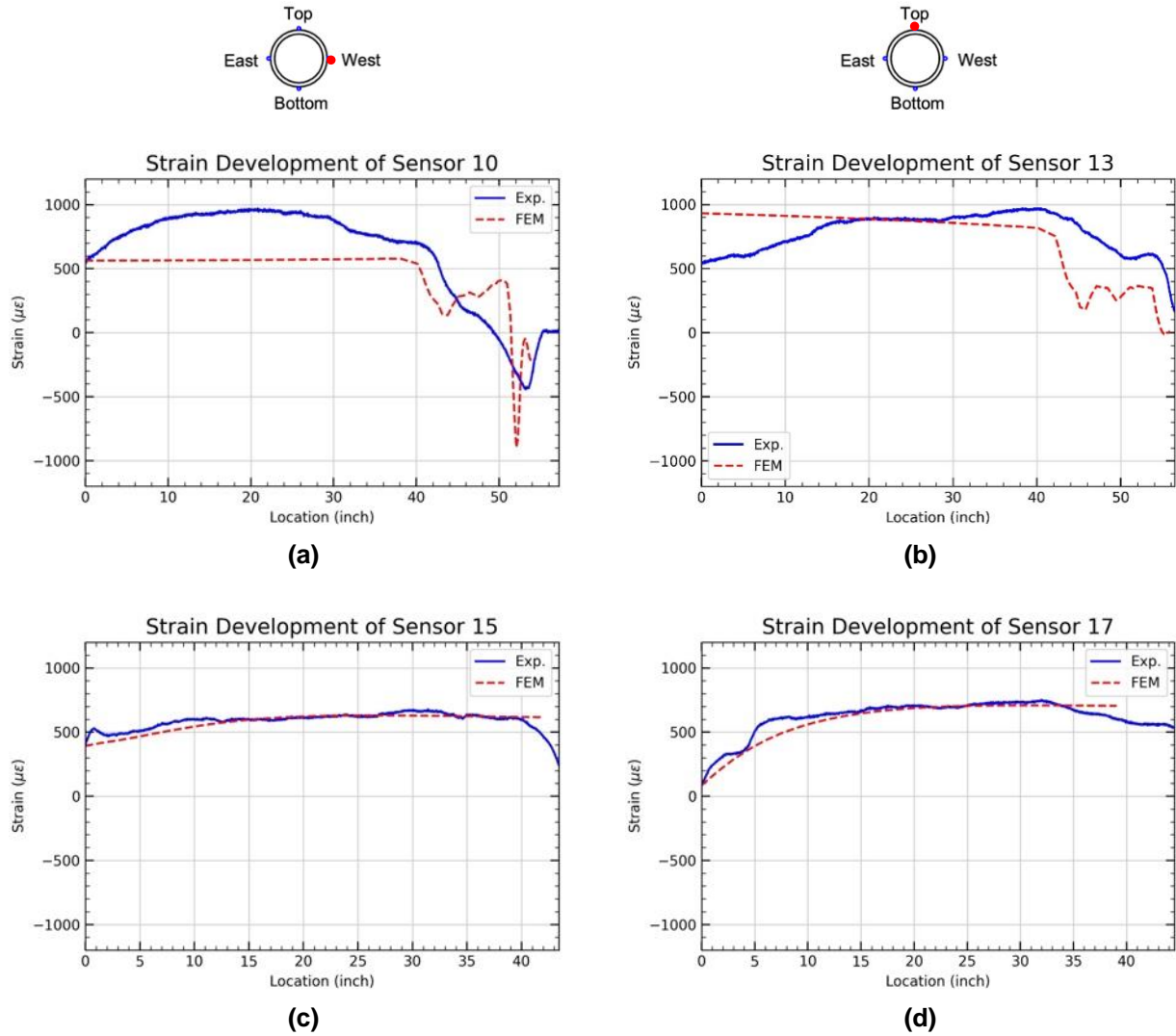


(c)



(d)

**Figure 5-12 Comparison of hoop strain results from FE simulation and experiment under 170-kip loading condition of test 2. (a) sensor on the bell pipe (b) sensor at the mid location of bell (c) sensor on top of the locking segments on the bell (d) sensor on the spigot**



**Figure 5-13 Comparison of axial strain results from FE simulation and experiment under 170-kip loading condition of test 2. (a) West side of bell pipe, (b) Top side of bell pipe, (c) West side of spigot, (d) Top side of the spigot**



## 6 Conclusions

This report describes the results of the experiments and finite element simulations of 8-inch TR-XTREME™ ductile iron pipe under direct tension force. The experiments were designed to test the pipe until severe damage or water leakage occurred. In Specimen 1, the test stopped at 188-kip loading force because of a failure of the weld bead on the spigot, which was responsible for the force transfer. No severe damage or water leakage was observed. In Specimen 2, the pipe failed at 174-kip loading force with a crack on the bell near the locking segments position. However, no water leakage was observed at this stage. Instead, the water started to leak until the displacement reached 4.4 inches. It is worth noting that in both tests, the maximum tension loads met and exceeded the minimum pull-apart resistance of 136 kips specified by the manufacturer (U.S. Pipe, 2020).

Fiber optic sensors captured the axial and circumferential strain developments. By viewing the strain distribution, one can observe that the bell section was squashing and moving upwards in the cross-sectional plane. The largest strain developed near the boundary where the locking segments bear with the weld bead, resulting in tensile failure. The experimental results were then compared to the finite element model. The strain distribution and patterns match well between the experiments and the simulation, indicating that the proposed finite element model can predict the behavior of the bell-spigot joint under tensile forces. The proposed model can be used in future parametric studies and as a reference for the model of the split basin fault rupture tests and also the additional pipe design guidance.

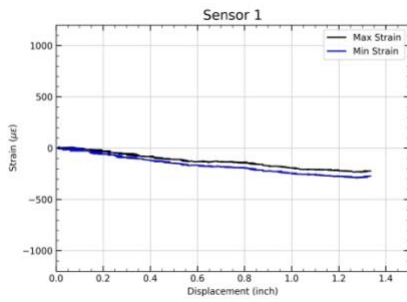
## 7 References

- U.S. Pipe. (2020). TR XTREME [Brochure]. [https://www.uspipe.com/wp-content/uploads/2020/12/USP\\_TR\\_XTREME\\_Brochure\\_03-03-2020-for-web.pdf?fbclid=IwAR2n950mDSY8OQ39WFCoVzV8WWoNmk\\_ae88eCPNjQym1okpuRK7mLp6absE](https://www.uspipe.com/wp-content/uploads/2020/12/USP_TR_XTREME_Brochure_03-03-2020-for-web.pdf?fbclid=IwAR2n950mDSY8OQ39WFCoVzV8WWoNmk_ae88eCPNjQym1okpuRK7mLp6absE)
- Wu, J., Jiang, H., Su, J., Shi, B., Jiang, Y., & Gu, K. (2015). Application of distributed fiber optic sensing technique in land subsidence monitoring. *Journal of Civil Structural Health Monitoring*, 5(5), 587-597.
- LUNA inc. (2022). ODiSI 6000 Series Optical Distributed Sensor Interrogators. Retrieved from <https://lunainc.com/sites/default/files/assets/files/data-sheet/Luna%20ODiSI%206000%20Data%20Sheet.pdf>
- ABAQUS (2020). <https://www.3ds.com/support/hardware-and-software/simulia-system-information/abaqus-2020/>.

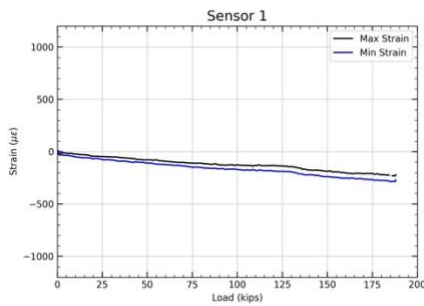
# Appendix A: Fiber Optic Sensors Result

The results from the distributed fiber optic sensors are demonstrated herein. Plot (a) shows the relation between the strain and displacement at the locations where the maximum and minimum strains happened, respectively. Similarly, plot (b) shows the strain versus displacement at both of the points. Plot (c) demonstrates the strain development along the sensors at the maximum loading condition (i.e., 188 kips for test 1 and 174 kips for test 2).

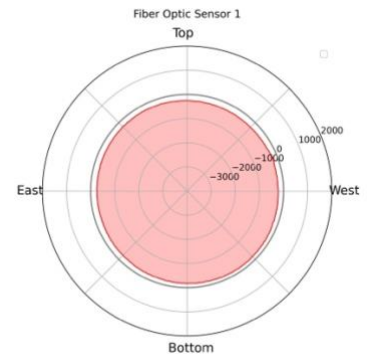
## (a) Specimen 1



(a) Strain vs displacement

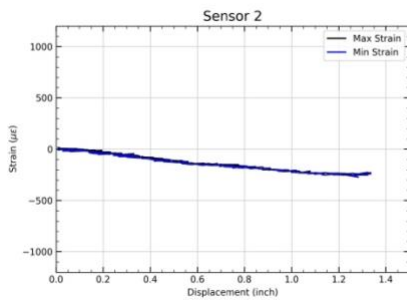


(b) Strain vs load

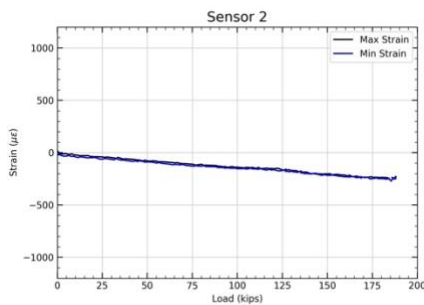


(c) Strain distribution at max. force condition

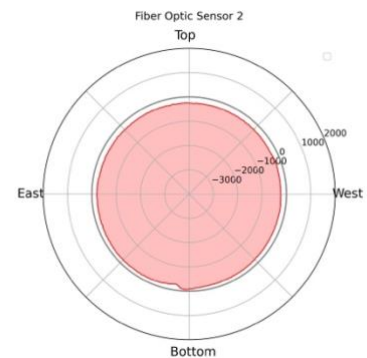
Figure A-1 Fiber optic Sensor 1 results



(a) Strain vs displacement

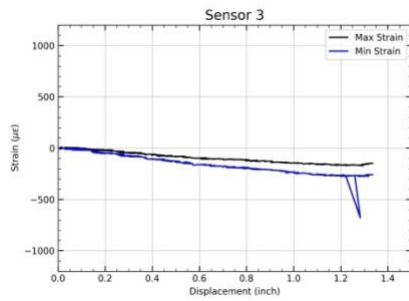


(b) Strain vs load

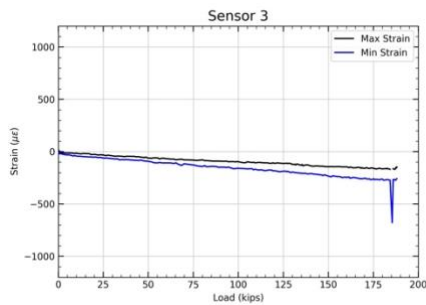


(c) Strain distribution at max. force condition

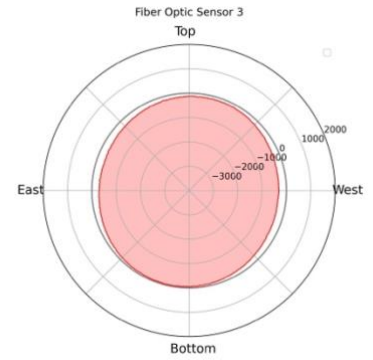
Figure A-2 Fiber optic Sensor 2 results



(a) Strain vs displacement

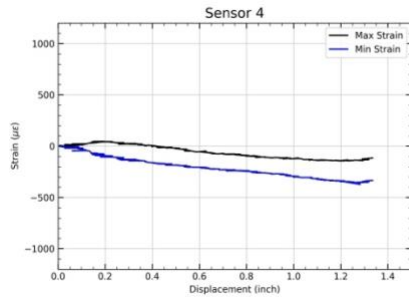


(b) Strain vs load

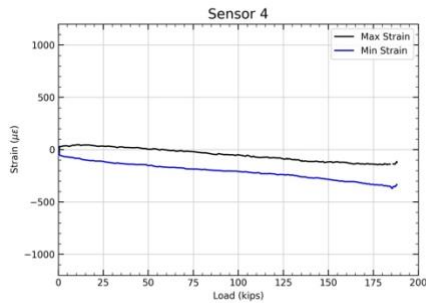


(c) Strain distribution at max. force condition

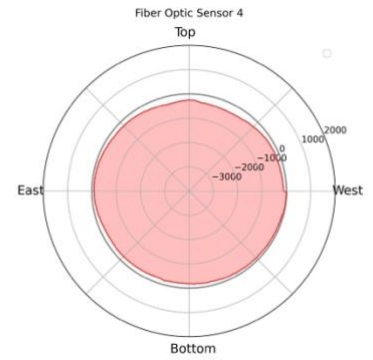
**Figure A-3 Fiber optic Sensor 3 results**



(a) Strain vs displacement

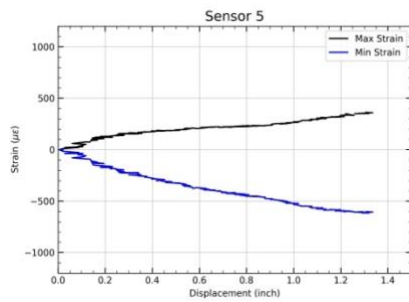


(b) Strain vs load

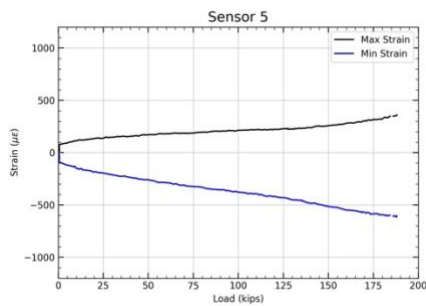


(c) Strain distribution at max. force condition

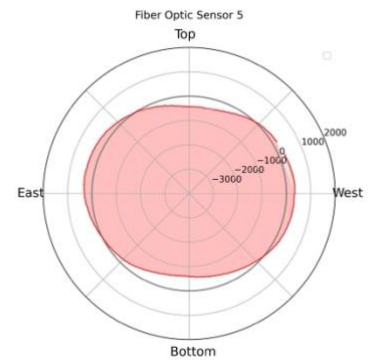
**Figure A-4 Fiber optic Sensor 4 results**



(a) Strain vs displacement

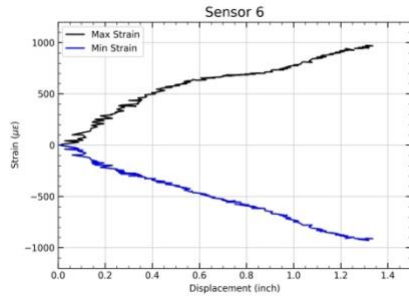


(b) Strain vs load

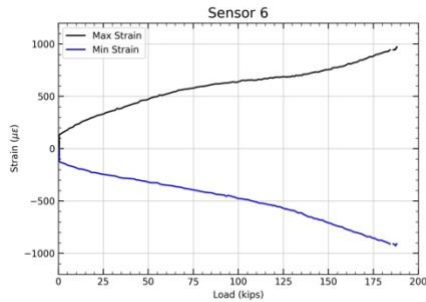


(c) Strain distribution at max. force condition

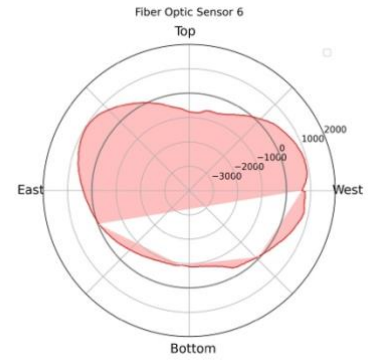
**Figure A-5 Fiber optic Sensor 5 results**



(a) Strain vs displacement

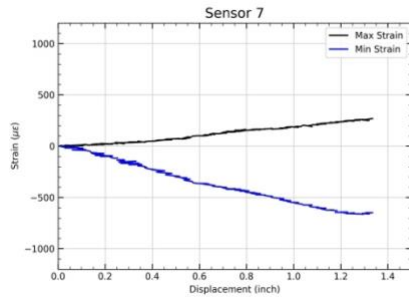


(b) Strain vs load

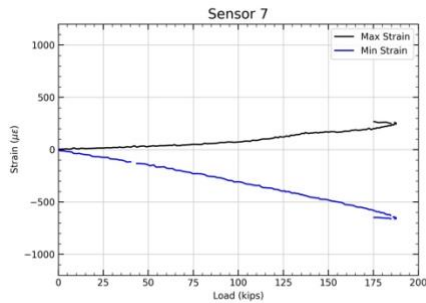


(c) Strain distribution at max. force condition

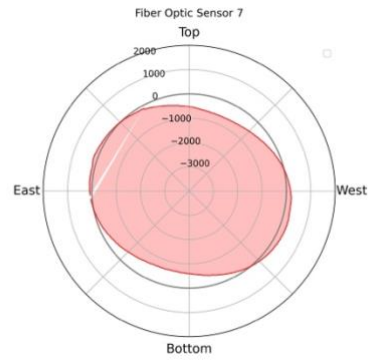
**Figure A-6 Fiber optic Sensor 6 results**



(a) Strain vs displacement

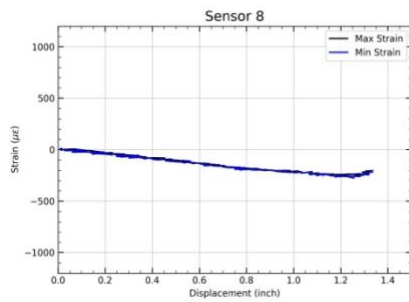


(b) Strain vs load

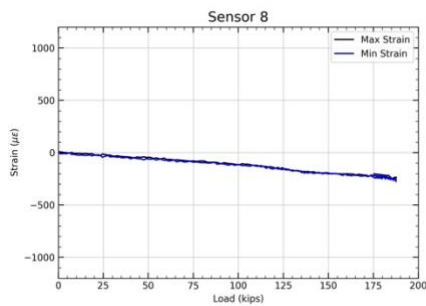


(c) Strain distribution at max. force condition

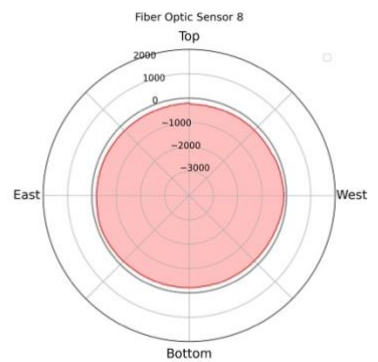
**Figure A-7 Fiber optic Sensor 7 results**



(a) Strain vs displacement

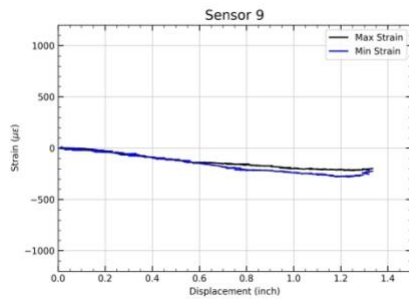


(b) Strain vs load

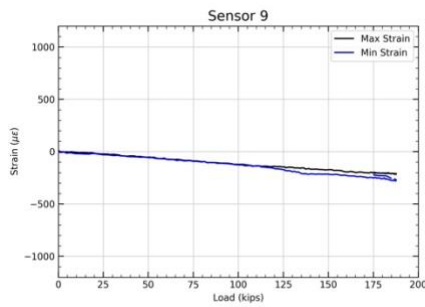


(c) Strain distribution at max. force condition

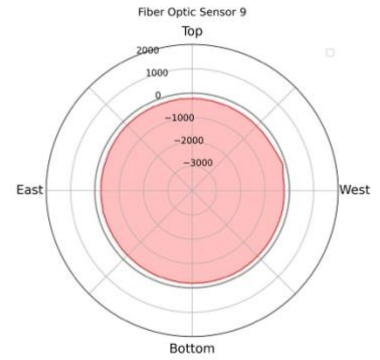
**Figure A-8 Fiber optic Sensor 8 results**



(a) Strain vs displacement

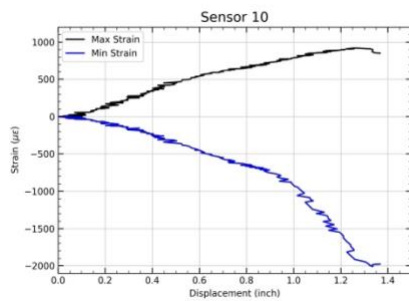


(b) Strain vs load

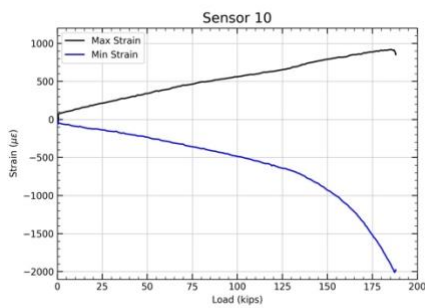


(c) Strain distribution at max. force condition

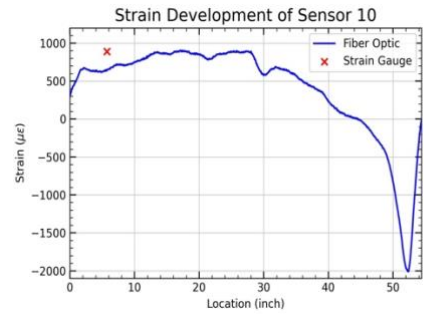
**Figure A-9 Fiber optic Sensor 9 results**



(a) Strain vs displacement

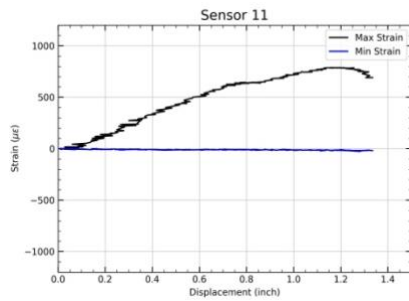


(b) Strain vs load

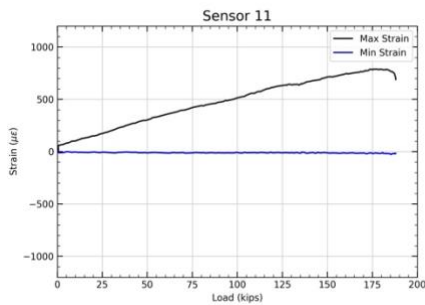


(c) Strain distribution at max. force condition

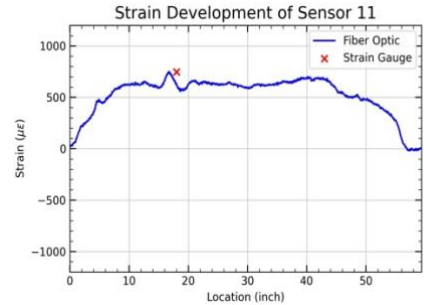
**Figure A-10 Fiber optic Sensor 10 results**



(a) Strain vs displacement

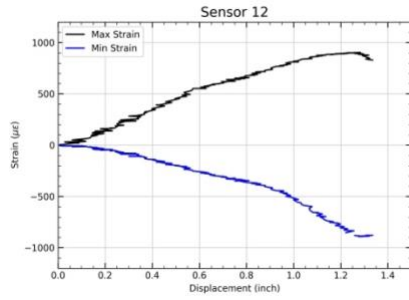


(b) Strain vs load

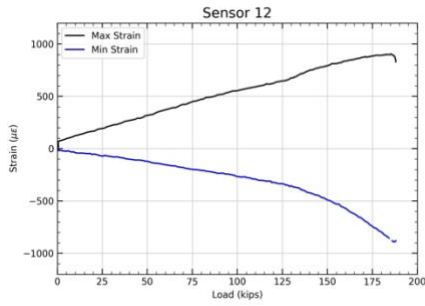


(c) Strain distribution at max. force condition

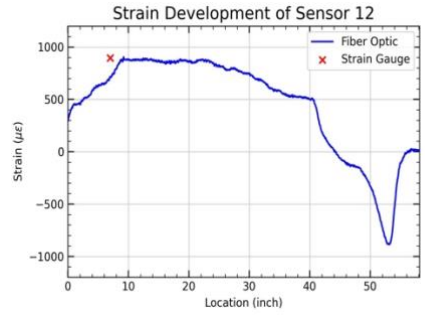
**Figure A-11 Fiber optic Sensor 11 results**



(a) Strain vs displacement

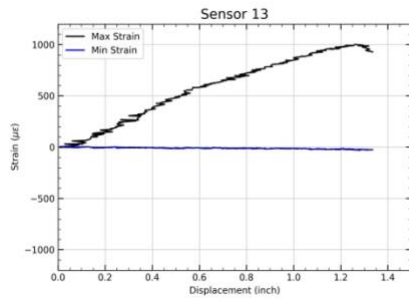


(b) Strain vs load

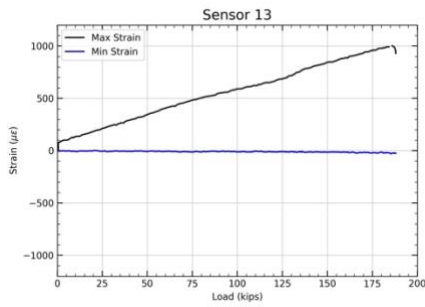


(c) Strain distribution at max. force condition

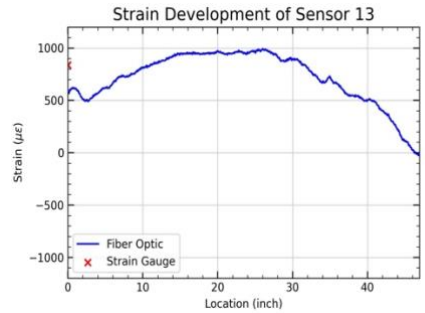
**Figure A-12 Fiber optic Sensor 12 results**



(a) Strain vs displacement

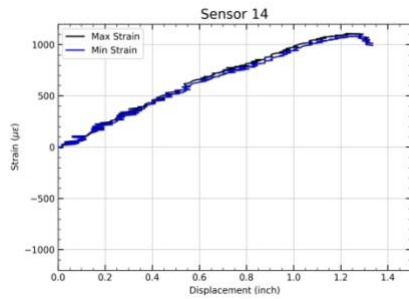


(b) Strain vs load

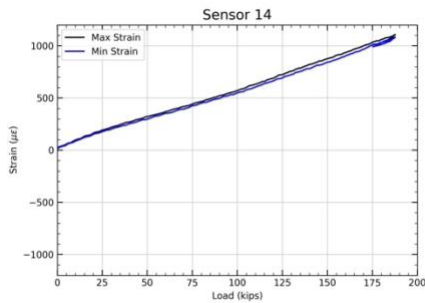


(c) Strain distribution at max. force condition

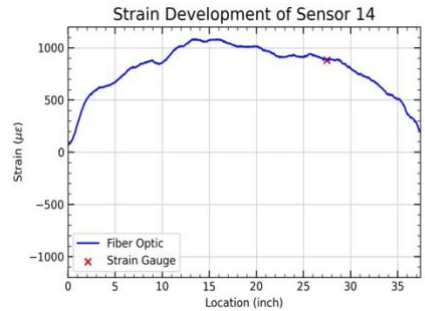
**Figure A-13 Fiber optic Sensor 13 results**



(a) Strain vs displacement

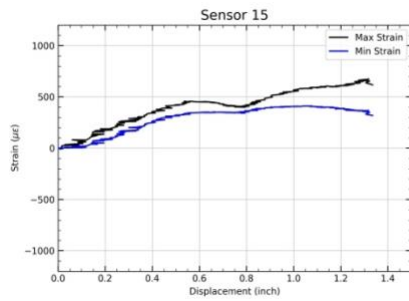


(b) Strain vs load

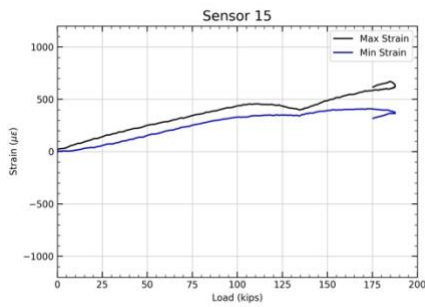


(c) Strain distribution at max. force condition

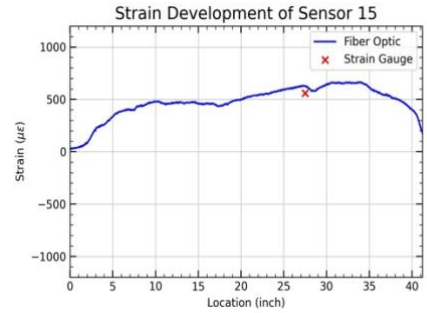
**Figure A-14 Fiber optic Sensor 14 results**



(a) Strain vs displacement

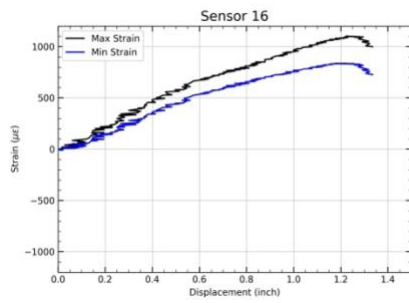


(b) Strain vs load

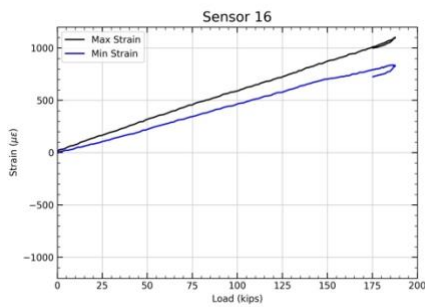


(c) Strain distribution at max. force condition

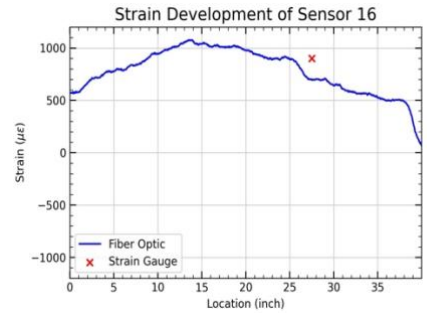
**Figure A-15 Fiber optic Sensor 15 results**



(a) Strain vs displacement

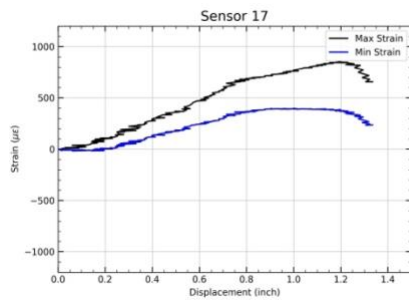


(b) Strain vs load

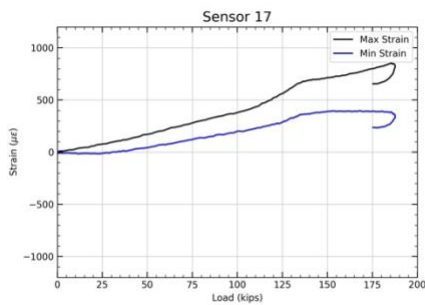


(c) Strain distribution at max. force condition

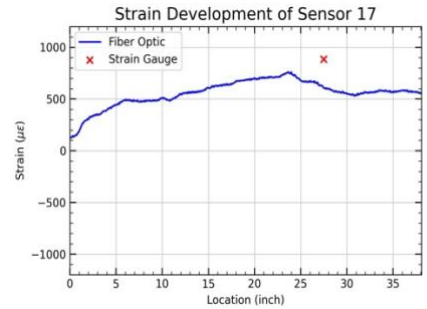
**Figure A-16 Fiber optic Sensor 16 results**



(a) Strain vs displacement



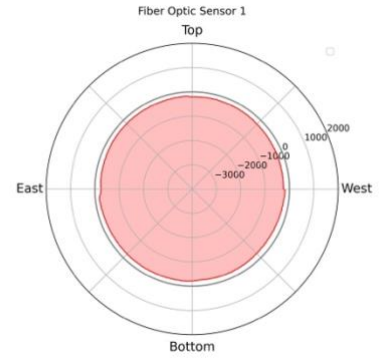
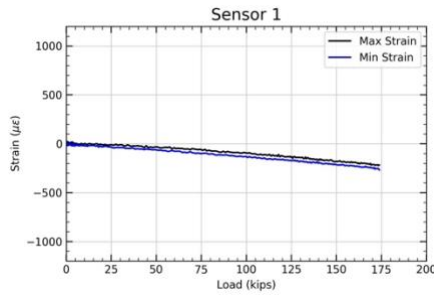
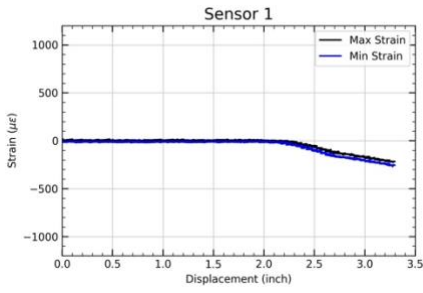
(b) Strain vs load



(c) Strain distribution at max. force condition

**Figure A-17 Fiber optic Sensor 17 results**

**(b) Specimen 2**

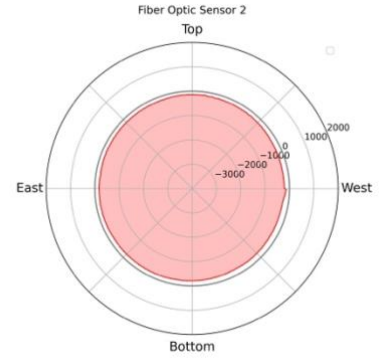
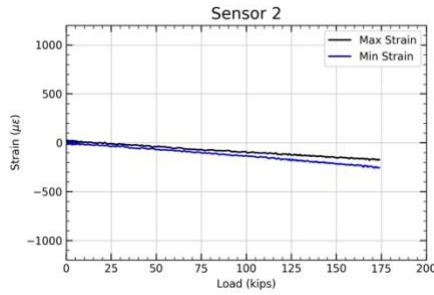
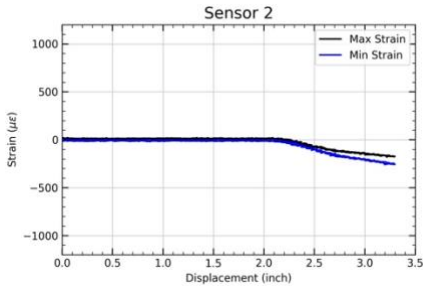


(d) Strain vs displacement

(e) Strain vs load

(f) Strain distribution at max. force condition

**Figure A-1 Fiber optic Sensor 1 results**

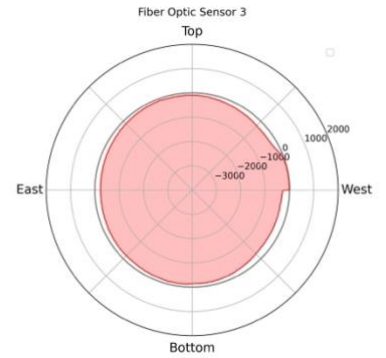
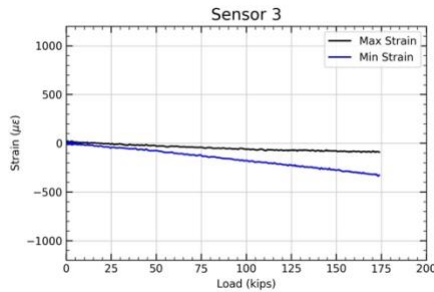
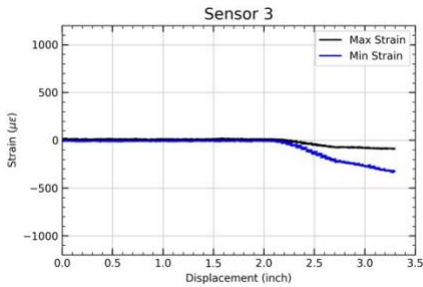


(d) Strain vs displacement

(e) Strain vs load

(f) Strain distribution at max. force condition

**Figure A-2 Fiber optic Sensor 2 results**



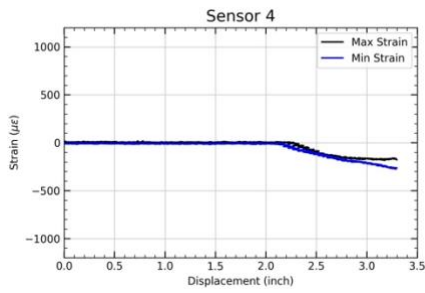
(d) Strain vs displacement

(e) Strain vs load

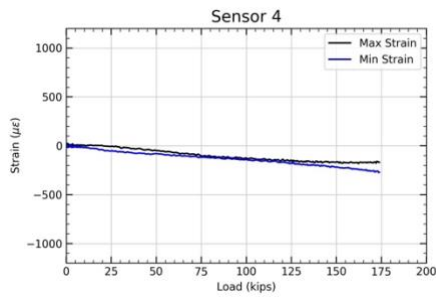
(f) Strain distribution at max. force condition

**Figure A-3 Fiber optic Sensor 3 results**

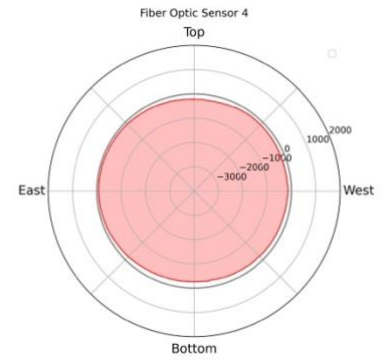




(d) Strain vs displacement

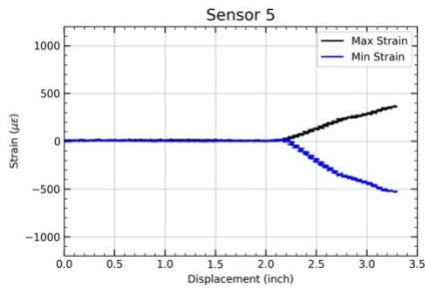


(e) Strain vs load

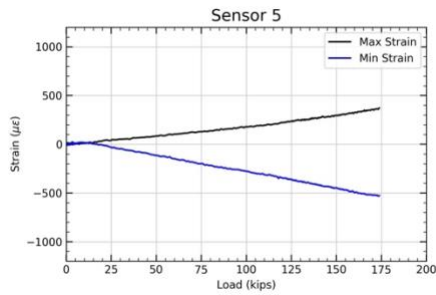


(f) Strain distribution at max. force condition

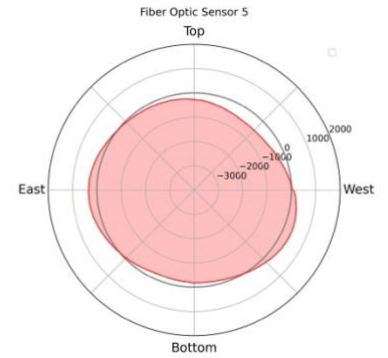
**Figure A-4 Fiber optic Sensor 4 results**



(d) Strain vs displacement

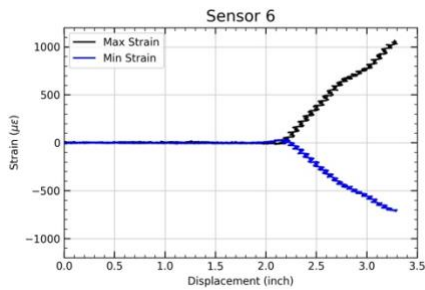


(e) Strain vs load

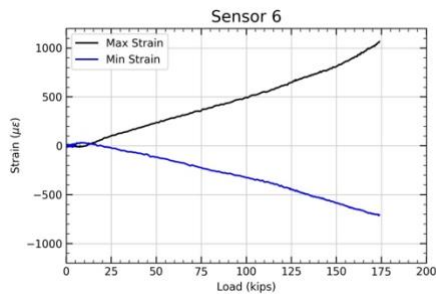


(f) Strain distribution at max. force condition

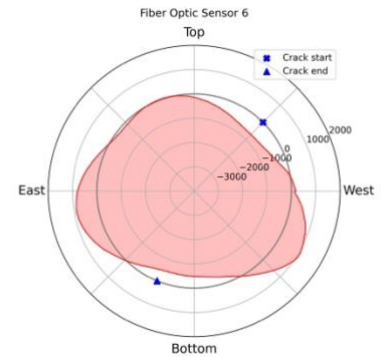
**Figure A-5 Fiber optic Sensor 5 results**



(d) Strain vs displacement

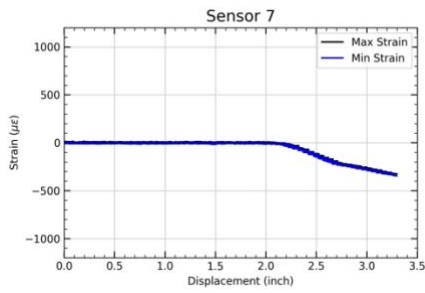


(e) Strain vs load

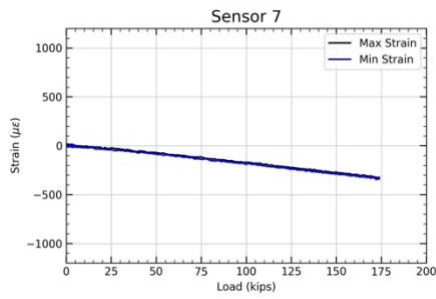


(f) Strain distribution at max. force condition

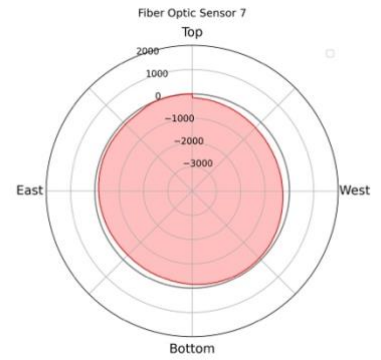
**Figure A-6 Fiber optic Sensor 6 results**



(d) Strain vs displacement

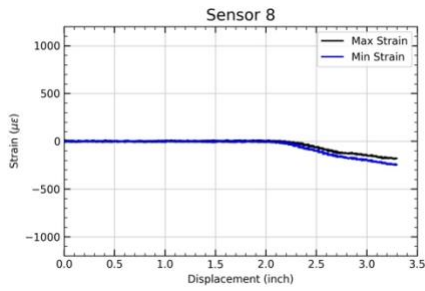


(e) Strain vs load

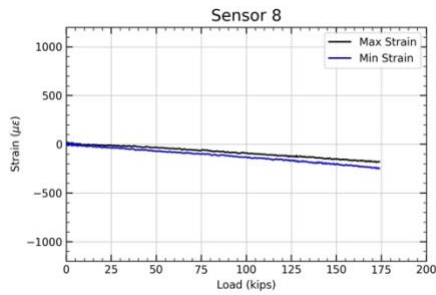


(f) Strain distribution at max. force condition

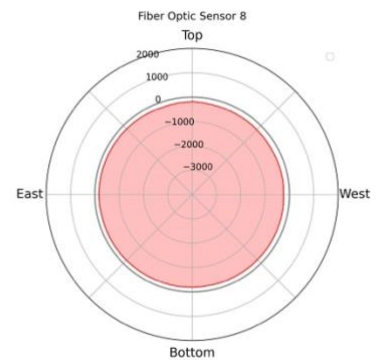
**Figure A-7 Fiber optic Sensor 7 results**



(d) Strain vs displacement

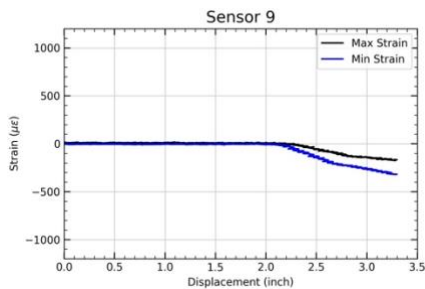


(e) Strain vs load

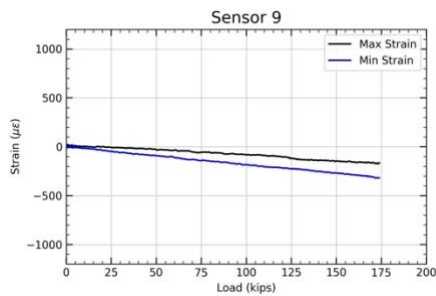


(f) Strain distribution at max. force condition

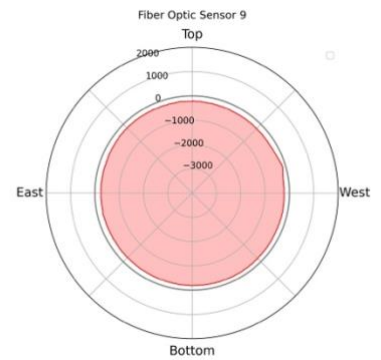
**Figure A-8 Fiber optic Sensor 8 results**



(d) Strain vs displacement

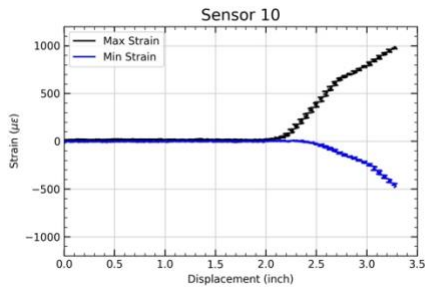


(e) Strain vs load

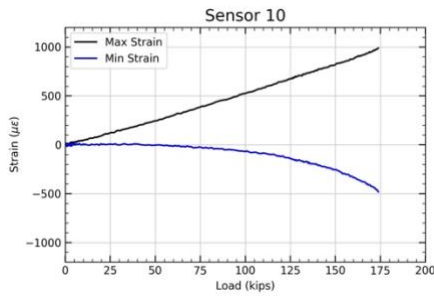


(f) Strain distribution at max. force condition

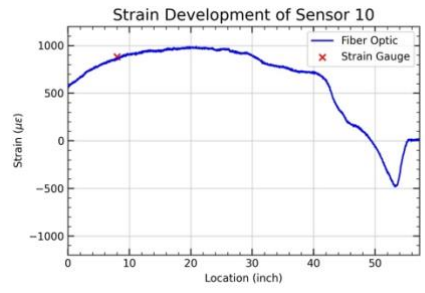
**Figure A-9 Fiber optic Sensor 9 results**



(d) Strain vs displacement

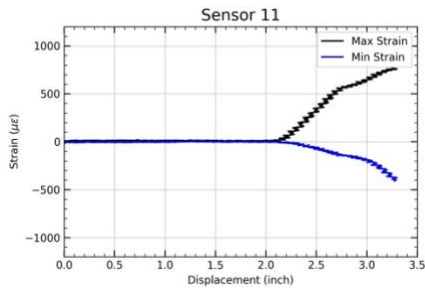


(e) Strain vs load

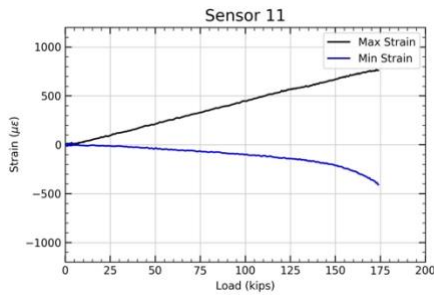


(f) Strain distribution at max. force condition

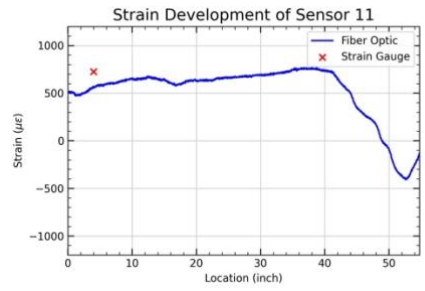
**Figure A-10 Fiber optic Sensor 10 results**



(d) Strain vs displacement

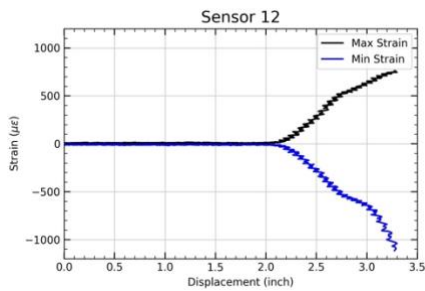


(e) Strain vs load

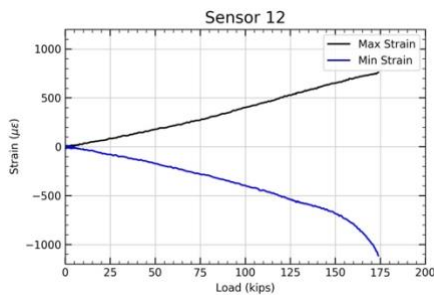


(f) Strain distribution at max. force condition

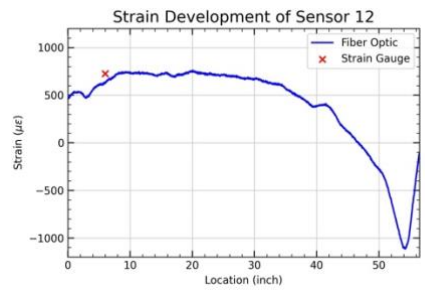
**Figure A-11 Fiber optic Sensor 11 results**



(d) Strain vs displacement

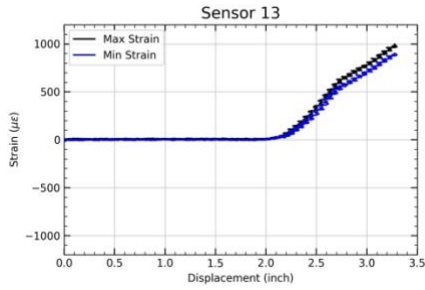


(e) Strain vs load

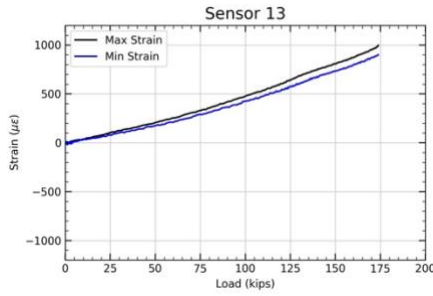


(f) Strain distribution at max. force condition

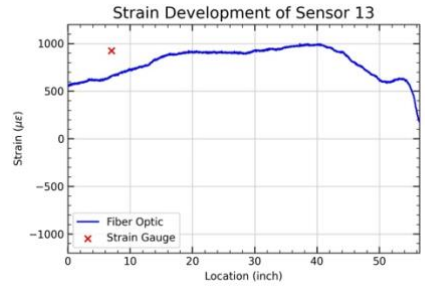
**Figure A-12 Fiber optic Sensor 12 results**



(d) Strain vs displacement

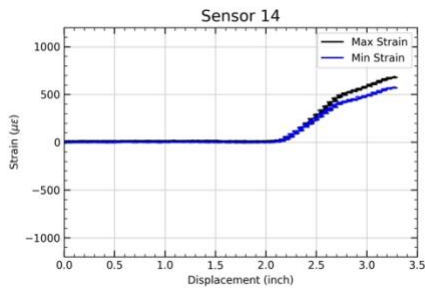


(e) Strain vs load

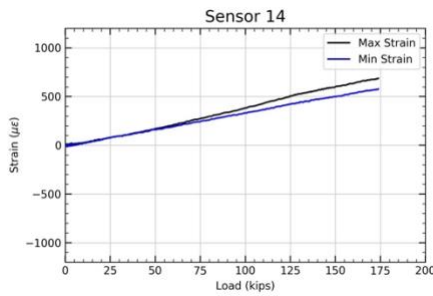


(f) Strain distribution at max. force condition

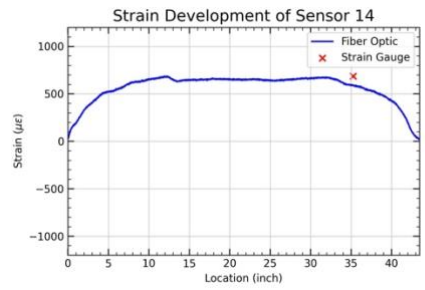
**Figure A-13 Fiber optic Sensor 13 results**



(d) Strain vs displacement

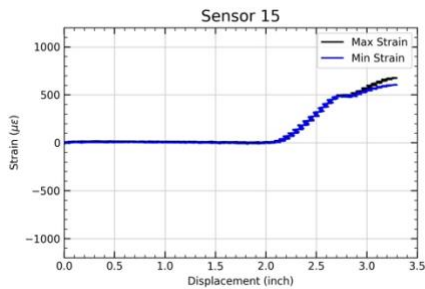


(e) Strain vs load

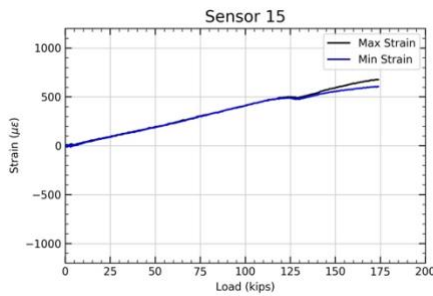


(f) Strain distribution at max. force condition

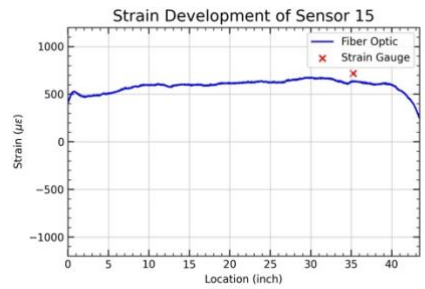
**Figure A-14 Fiber optic Sensor 14 results**



(d) Strain vs displacement

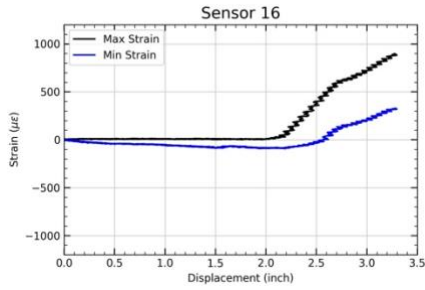


(e) Strain vs load

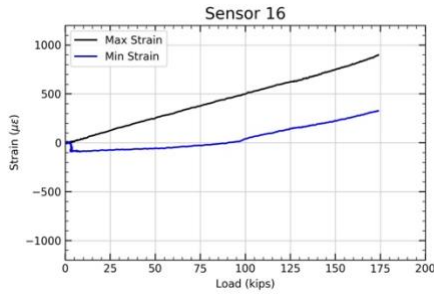


(f) Strain distribution at max. force condition

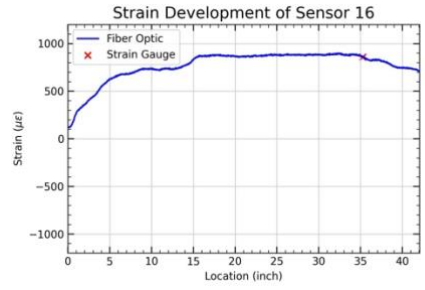
**Figure A-15 Fiber optic Sensor 15 results**



(d) Strain vs displacement

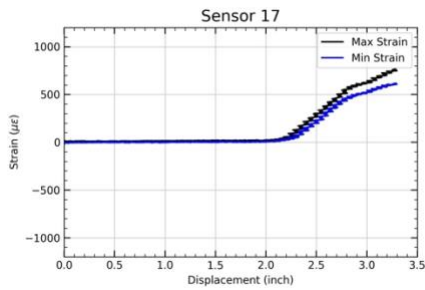


(e) Strain vs load

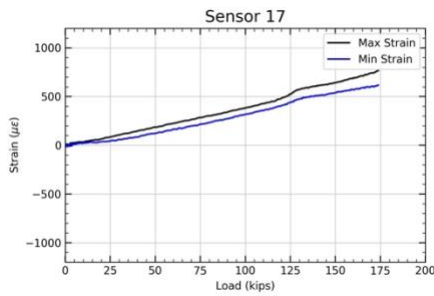


(f) Strain distribution at max. force condition

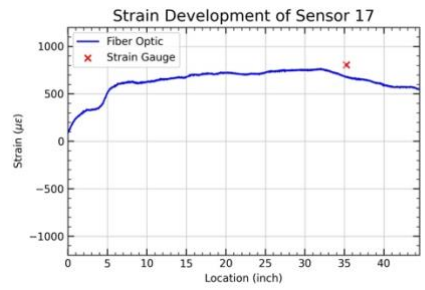
**Figure A-16 Fiber optic Sensor 16 results**



(d) Strain vs displacement



(e) Strain vs load



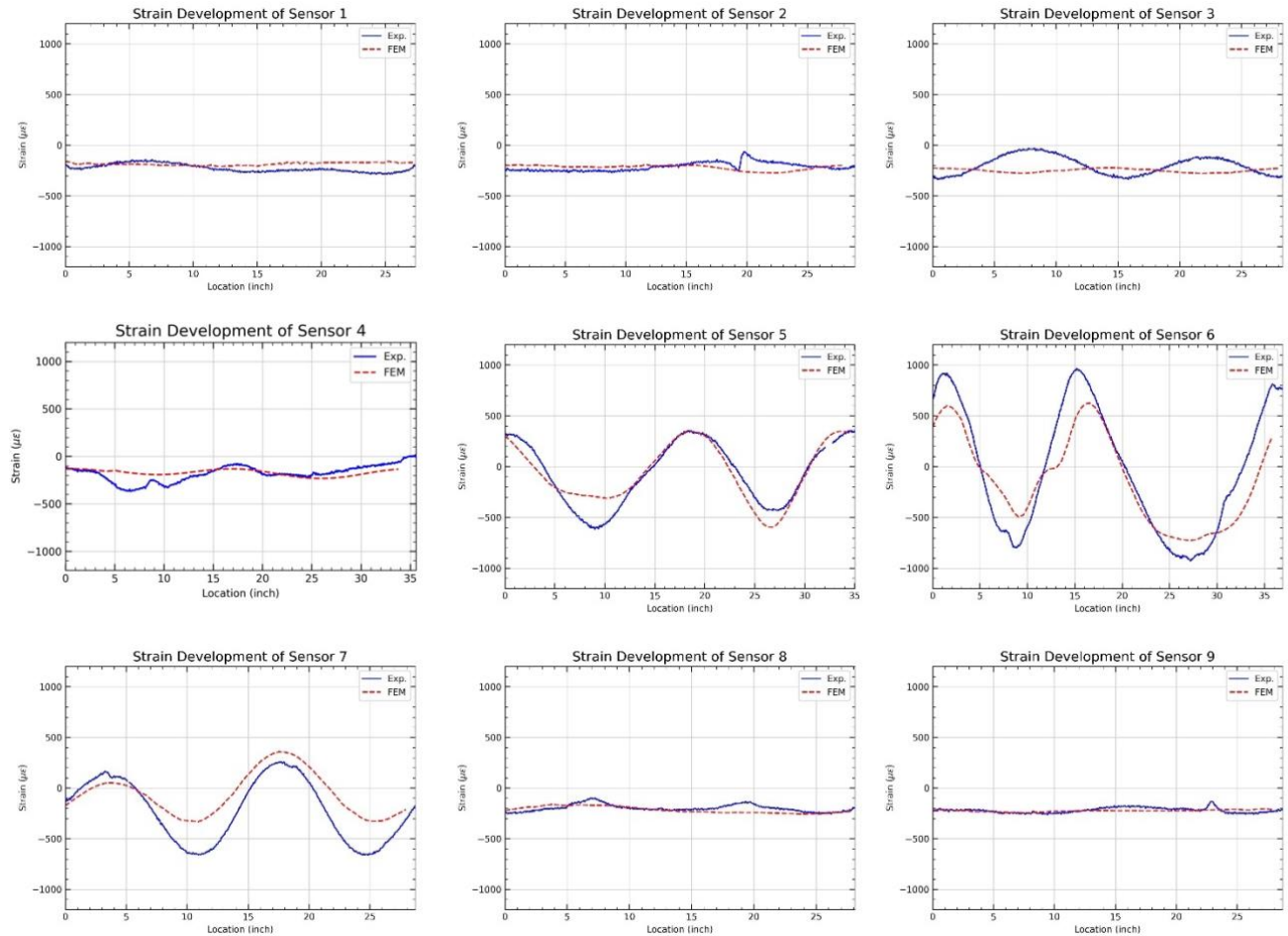
(f) Strain distribution at max. force condition

**Figure A-17 Fiber optic Sensor 17 results**

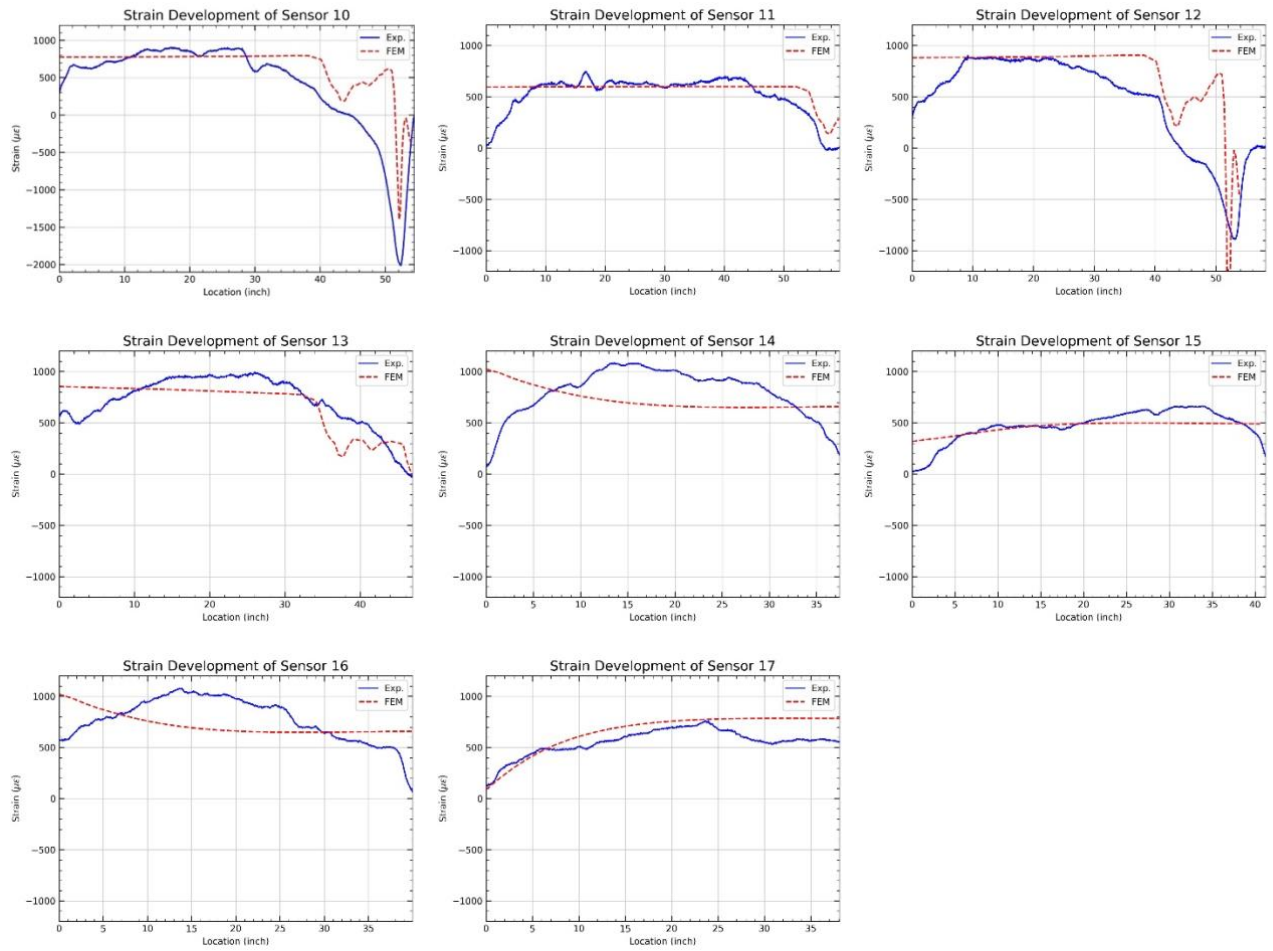
# Appendix B: Comparison of FE simulation results and experimental results

The experimental data were compared to the results from FE model. All the comparison results are shown in this section.

## (a) Specimen 1

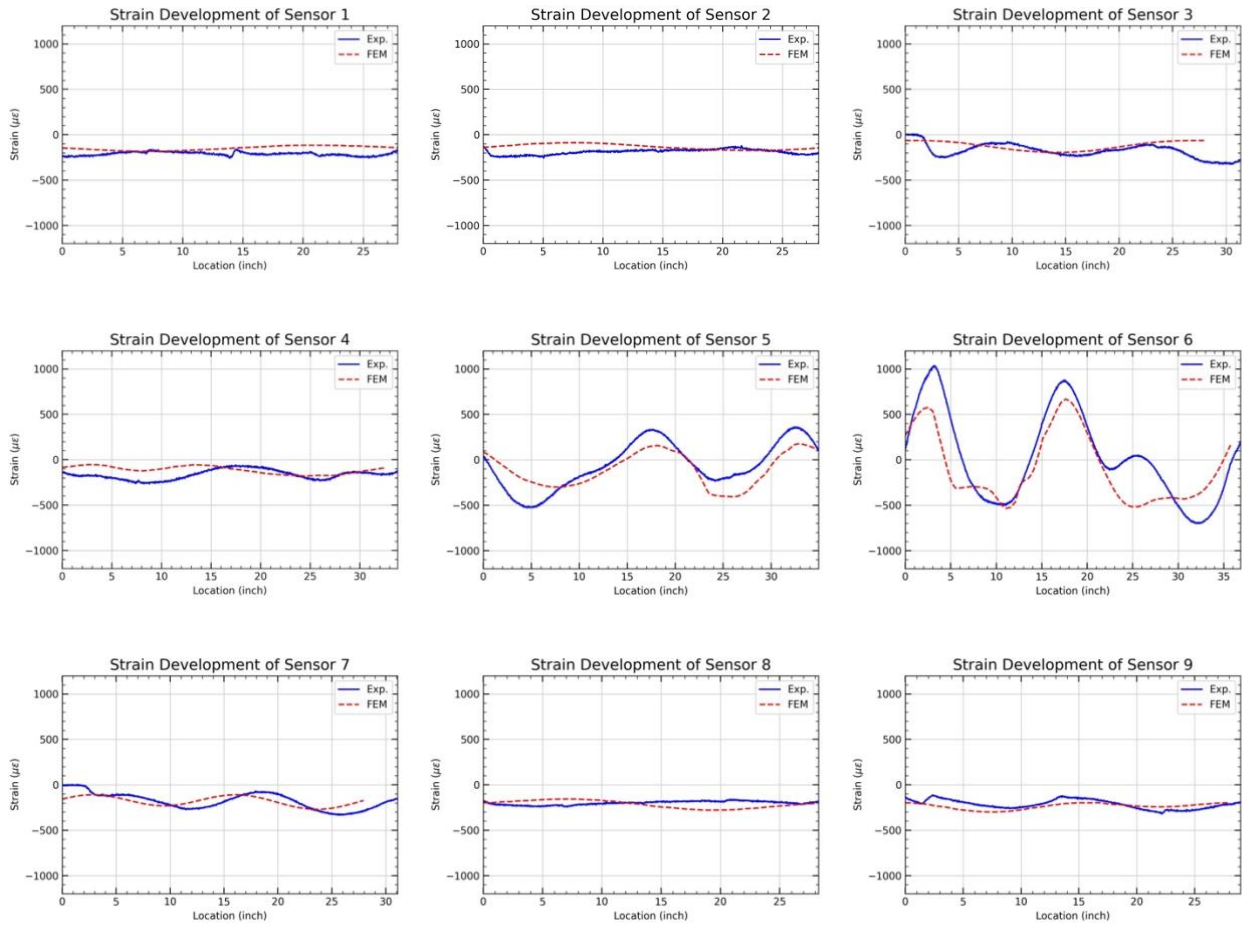


**Figure B-1 Comparison of experimental and FEM results of hoop strains under 185-kips axial force of test 1**



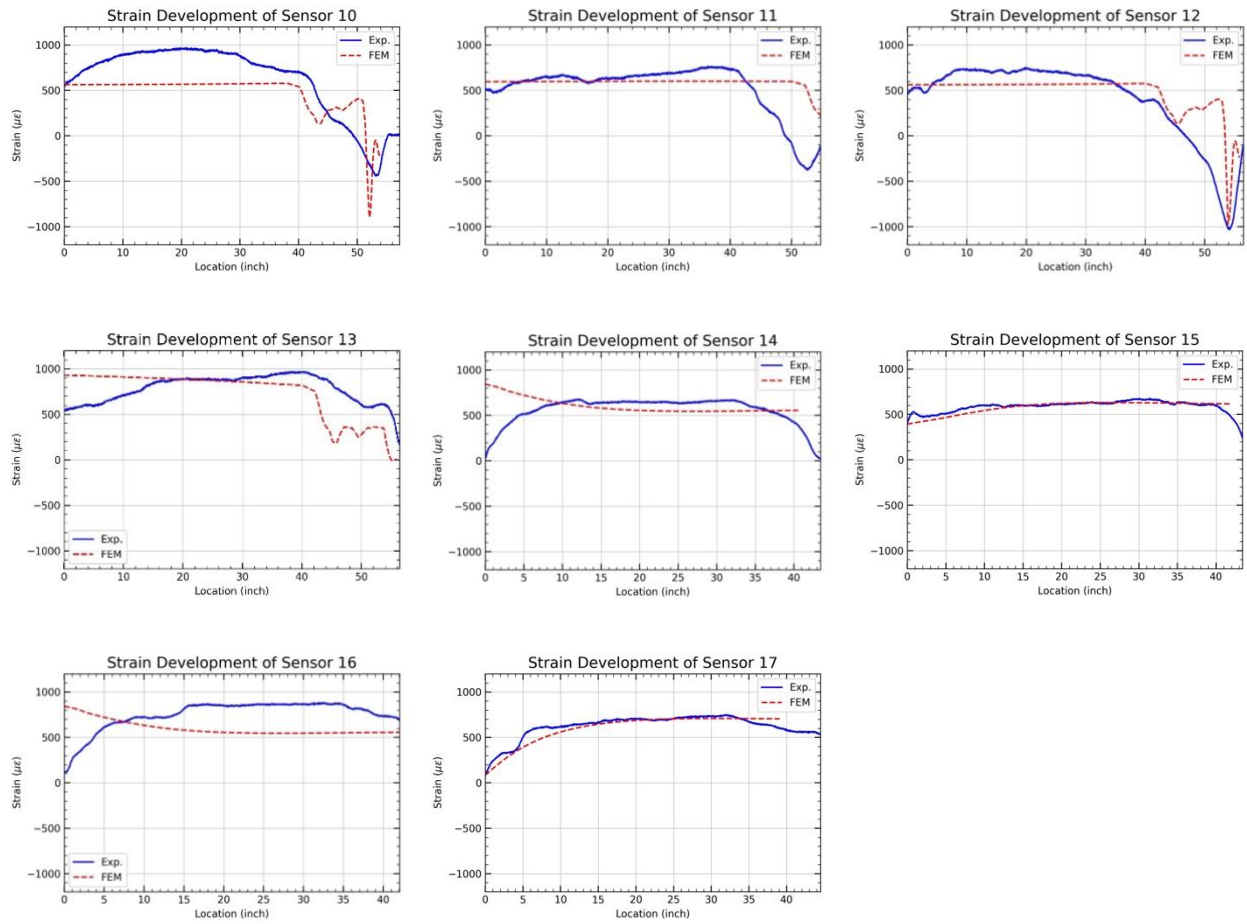
**Figure B-2 Comparison of experimental and FEM results of axial strains under 185-kips axial force of test 1**

**(b) Specimen 2**



**Figure B-3 Comparison of experimental and FEM results of hoop strains under 170-kips axial force of test 2**





**Figure B-4 Comparison of experimental and FEM results of axial strains under 170-kips axial force of test 2**